UNIVERSITEIT ANTWERPEN

Faculteit Wetenschappen

Departement Fysica

Vortex matter in a superconducting disk with magnetic coating

A theoretical study of the superconducting state, vortex configurations, and critical parameters of a superconductor-ferromagnet coaxial hybrid

Eindverhandeling ingediend tot het bekomen van de
meestergraad nanofysica

Mohammad Tauhidul Islam Rakib

Promotor: Prof. Dr. F. M. Peeters
Co-promotor: Dr. Milorad Milošević

Academiejaar 2005-2006

Contents

1

Introduction

In ongoing technological attempts in miniaturization of electronic circuits superconductors show certain prospects due to their particular electronic and magnetic properties. In that respect, and after recent developments in nano-fabrication techniques, mesoscopic superconducting heterostructures have received immense attention in both experimental and theoretical physics.

The size of samples we refer to as "mesoscopic" is actually comparable to the coherence length ξ and the magnetic penetration depth λ, which depend on the material but are both below micrometer. It has already been found that the behavior of such submicron samples in an external magnetic field is strongly influenced by sample geometry and boundary conditions [1]. One can easily assume that the critical phenomena and the vortex configurations of such samples become even richer if external magnetic field is not homogeneous, but varies over the sample.

For that reason, in the last decade, both experimental and theoretical analysis of superconductor/ferromagnet heterostructures have taken keen attention in the scientific community (see Refs. [2, 3, 4, 6, 7] and references therein). For a ferromagnetic dot or current loop placed on top of the superconductor, the local magnetic field profile becomes strongly inhomogeneous (with zero

average). That inhomogeneity of the field applied to the super-conductor, several unique phenomena were found, such as existence of vortex-antivortex pairs, field-induced superconductivity, field-polarity-dependent vortex pinning, novel phase transitions between states with different angular momenta and different constituents in terms of giant- and multi-vortices, and other [3, 5, 4, 7].

Following the progress in fabricating of hybrid nanostructures and motivated by above recent investigations, we study here the properties of a mesoscopic disk surrounded by a ferromagnetic ring. A special attention has been paid to avoid the proximity effect between the superconductor and the ferromagnetic element, considering them separated by a thin oxide layer to ensure that the interaction between SC and FM has purely magnetic character. The resulting magnetic field profile has an important property that the field is pronounced close to the edge of the disk and decays fast towards the center of the superconducting structure. The main concern of this thesis is to study the influence of this spatial non-homogeneous field profile on the superconducting state of the mesoscopic disk. Particularly, in such a hybrid sample, ferromagnet strongly alerts the vortex structure in its neighborhood, and influences in a non-trivial way the critical parameters of the device.

This thesis consists of five chapters:

Chapter 1 gives a short introduction of superconductivity and mesoscopic superconducting structures, and the corresponding theory. We present the Ginzburg-Landau equations and chosen boundary conditions, which form the theoretical framework of this thesis. Type-I and type-II superconductors and the characteristic lengths are introduced. A general discussion on giant-vortex state, multi-vortex state and vorticity are provided. In the second part we also discuss briefly the fundamentals, i.e. the local magnetic field, Cooper-pair density and supercurrent, as well as the Gibbs free energy, as a function of magnetic field in a mesoscopic superconducting disk exposed to a homogeneous magnetic field.

Chapter 2 presents a theoretical overview of main aspects of magnetism and magnetostatic calculations. Both analytical and numerical approaches are presented, and compared, for the calculation of the stray magnetic field of a ferromagnetic ring.

Chapter 3 describes the superconducting state of a thin mesoscopic superconducting disk with a ferromagnetic ring around, using Ginzburg-Landau theory, within the 1-dimensional approach developed by Schweigert and Peeters [1]. Cylindrical symmetry of the superconducting state is assumed in this approach, and we investigate the stable vortex states as a function of applied field, radius of the disk, and parameters of the magnet.

Chapter 4 deals with results from previous chapter, but now within the 2-dimensional approach, where no particular symmetry is taken *a priori*. Depending on the disk radius and the properties of the magnetic stray field profile, we study the vortex matter in the sample.

Chapter 5 reports on the influence of homogeneous magnetic field on our sample, i.e. the superconducting disk with ferromagnetic ring around. Field-polarity dependent vortex structure and enhancement of critical field of the sample are studied. Also, the formation of vortex shells and effective control of "magic numbers" in the sample are addressed here.

1.1　INTRODUCTION TO SUPERCONDUCTIVITY

The ability to carry electric current without resistance has puzzled the scientific community since the first observation of the phenomenon in 1911. Experimental and theoretical physicists all over the world have put a considerable amount of effort into understanding the microscopic origin of the complete loss of electrical resistivity that takes place in some materials, named superconductors, when they are cooled to sufficiently low temperatures (transition temperature T_c).

About half of the metallic elements and also a large number of alloys and intermetallic compounds have been found to superconduct at low temperatures. Currently there are about 29 simple elements that exhibit superconductivity at normal pressure with critical temperatures varying between 0.0003K for rhodium (Rh) and 9.25K for niobium (Nb). Many other elements, such as Si and Ge, become superconductors when subjected to very high pressures. From a technological point of view, the alloy NbTi (T_c = 10K) and the intermetallic compound Nb_3Ge (T_c = 18K) are

particularly important. Most wires and commercially available superconductor devices are manufactured from these materials. It is interesting that good conductors such as Cu, Ag, and Au are not observed to become superconductors. Neither are those transition and rare earth metals who possess a magnetic moment.

The low temperature required to maintain the material in the superconducting state is a limiting factor that has prevented many technological applications of superconductivity. On the other hand, *zero electrical resistance* is very beneficial for applications. Resistance is undesirable because it produces looses in the energy while flowing through the material. Zero electrical resistance means that no energy is lost as heat as the material conducts electricity - this has many applications like efficient electricity transportation, magnetic levitation, magnetic resonance imaging (MRI), synchrotrons and cyclotrons (particle colliders), fast electronic switches etc.

1.1.1   Historical overview

Discovery of superconductivity is one of the last great frontiers of science. In 1911 superconductivity was first observed in mercury by Dutch physicist Heike Kamerlingh Onnes of Leiden University [18]. In 1908, Onnes had become the first person to liquify helium, which resulted in the Noble prize in 1913. He was investigating the electrical properties of various substances at low temperatures. When he cooled mercury to the temperature of liquid helium, i.e., 4.2 K (-452F, -269C), its resistance suddenly disappeared (Fig. 1.1). He coined the name *superconductivity* for this phenomenon with extraordinary electrical properties (*perfect conductivity*). The same property were observed in some other metals, such as lead and tin.

In 1933, German researchers Walter Meissner and Robert Ochsenfeld discovered that a superconductor is more than a perfect conductor of electricity, as it also has an interesting magnetic property of excluding magnetic field when cooled through the critical temperature (Fig. 1.2) [19]. Namely the induced currents (persistent currents) generate a magnetic field inside the superconductor that just balances the field that would have otherwise penetrated the superconducting material, (Fig. 1.3). However this so-called Meissner effect is most effective against the magnetic field which
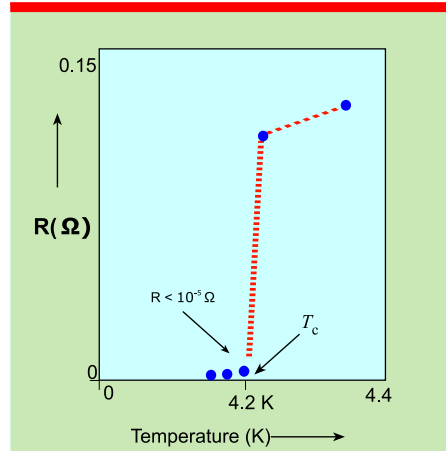
Fig. 1.1   The resistance of a specimen of mercury versus absolute temperature which marked the discovery of superconductivity. The electrical resistivity of mercury drops abruptly to zero at 4.2K (Ref. [18]).

is relatively small. If the magnetic field becomes too large, it penetrates the interior of the metal and the metal loses its superconductivity.

The first theory to describe the field expulsion was developed by the brothers London two years later in 1935 [20]. This theory proved to be useful for describing the superconducting behavior and vortex states in extreme type-II superconductors (see section-1.1.6). The London theory treats vortices classically, as point-like objects and does not take into account the finite size and the inner structure of the vortex.

A substantial progress was made by V. Ginzberg and L. Landau in 1950, who employed quantum mechanics and proposed a phenomenological theory to describe superconductivity in the presence of a magnetic field [21]. This theory combined Landau's theory of second-order phase transitions with a Schrödinger-like wave equation for superconductivity, and had a great success in explaining the macroscopic properties of superconductors.

In 1957, A. Abrikosov used the Ginzburg-Landau (GL) theory to predict a new quantum state, the 'mixed state' of type-II superconductors [22]. The mixed state in a type-II superconductor is characterized by failure of the Meissner effect: as the magnetic field penetrates the superconductor as individual flux tubes called
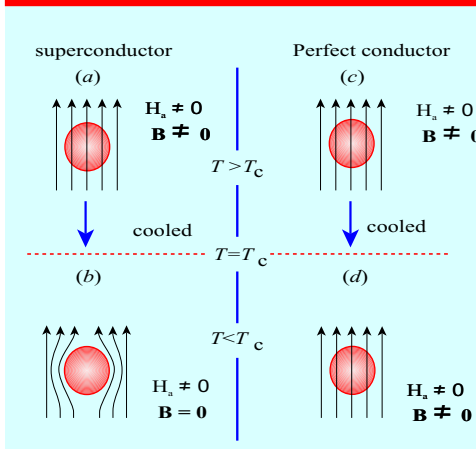
Fig. 1.2 Magnetic behavior of a superconductor and a perfect conductor in the presence of a constant magnetic field; the flux density B refers to the value inside the specimen. (a, c): the material is at a temperature $T > T_c$. Due to its finite resistivity, the flux lines penetrate the interior of the specimen. (b, d): For $T < T_c$, the superconductor excludes the magnetic flux from its interior, while the magnetic state of a perfect conductor does not change.

vorticity (each carrying the flux quantum $\Phi_0 = h/2e$) where superconductivity is locally destroyed. Moreover, vortices were found to array in a triangular lattice as the energy favorable configuration, later called the Abrikosov lattice. For there contributions to the theory of SC, V. Ginzburg and A. Abrikosov were awarded the Nobel prize for Physics in 2003.

Also in 1957, J. Bardeen, L. Cooper and J. Schrieffer made the major breakthrough in the field of superconductivity by describing its microscopic mechanism (see section-1.1.3)[23]. The BCS theory explained the superconducting current as a superfluid of ***Cooper pairs***, pairs of electrons interacting through the exchange of a phonon. For this work Bardeen, Cooper and Schrieffer received the Nobel Prize in 1972. Two years later, Gor'kov was able to show that the BCS theory reduced to the Ginzburg-Landau theory close to the critical temperature, i.e, the GL theory was in fact a limiting case of the microscopic theory [24].

Both theoretical and experimental studies seemed to be settled then until 1986. That year, Bednorz and M*ü*ller discovered the first high-T_c superconductor [25]. It was a layered copper oxide
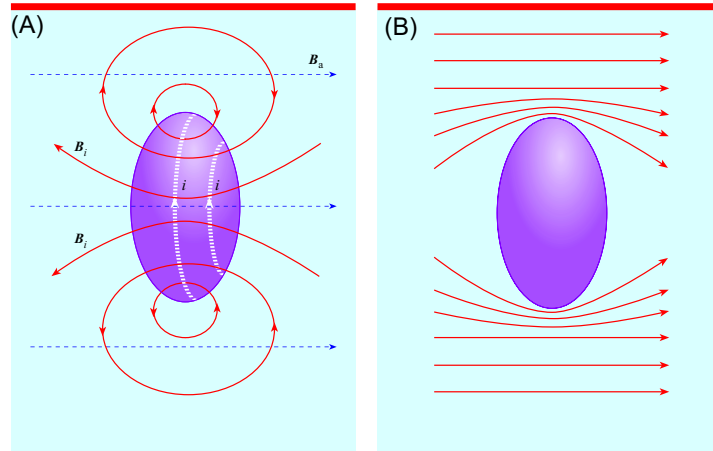
Fig. 1.3 (A) Magnetic flux distribution in a diamagnetic body such as a supercon-
ductor. When a magnetic field is applied to a superconductor, persistent currents i
circulate in the surface of the material in such a manner as to produce a flux density
$B_i = B_a$, which exactly cancels the flux inside the superconductor due to the applied
field. (B) Net distribution of magnetic flux in the vicinity of a diamagnetic body.

(cuprate) with T_c of 38K. Before this the highest critical temper-
ature was only 23K for Nb_3Ge. For their discovery, Bednorz and
M$\ddot{u}$ller received the Nobel prize in 1987.

Subsequently different cuprates have been found with increasing
critical temperature. By 1993, cuprates with a T_c of 133K at
atmospheric pressure were found ($HgBa_2Ca_2Cu_3O_8$) [16]. After
this discovery further efforts to find cuprates with higher T_c failed
until 2000, when a slight increase in the transition temperature
was detected for fluorinated Hg-1223 samples ($T_c = 138K$) [17].

The BCS theory was unable to describe many properties of the
high-T_c materials. The electron-phonon mechanism became ques-
tionable. New mechanisms, such as the so-called d-wave pairing,
has been proposed. But, at present, the question of why the high-
T_c superconductors have such high-T_c values is still unanswered.

1.1.2   The London theory

After the discovery of superconductivity, it took more then 20
years to develop the first phenomenological theor to describe the
phenomenon. It was proposed by brothers London in 1935 [20].

The first assumption of this theory is that, Newton's 2nd law can be written in the following form:

$$m^* \frac{d\vec{v}_s}{dt} = -e^* \vec{E}, \qquad (1.1)$$

where m^* is the mass of the supercurrent charge carriers, e^* is the charge of the carriers, $\vec{v}_s$ is the supercurrent velocity, and $\vec{E}$ is the applied electric field. If one takes the superconducting carrier density, then the above equation becomes,

$$\frac{\partial \vec{j}_s}{\partial t} = \frac{n_s e^2}{m^*} \vec{E}. \qquad (1.2)$$

With the inclusion of Faraday's law, one obtains the following relation:

$$\frac{\partial}{\partial t} \left[\vec{\nabla} \times \vec{j}_s + \frac{n_s e^2}{m^* c} \vec{H} \right] = 0. \qquad (1.3)$$

Such a result is true of any perfect conductor. However, notice that any temporally constant value of $\vec{j}_s$ and magnetic field $\vec{H}$ will satisfy the above relation. Hence, a magnetic field that penetrated the sample in the normal state would be locked into the interior of the crystal as it passed into the superconducting phase. This, of course, does not happen, so the London brothers final assumption was to restrict the family of solutions of the above equation to those that satisfy:

$$\vec{\nabla} \times \vec{j}_s = -\frac{n_s e^2}{m^* c} \vec{H}. \qquad (1.4)$$

This equation states that dissipationless supercurrents flow at the surface of the crystal to completely shield the sample interior from the external magnetic field. Moreover, the above relation also predicts that any magnetic flux initially passing through the crystal

will be completely expelled upon entering into the superconducting state.

The combination of Eq. (1.4) with the Maxwell equation for the magnetic field $\vec{\nabla} \times \vec{H} = 4\pi \vec{j}_s/c$ leads to

$$\vec{\nabla}^2 \vec{H} = \frac{1}{\lambda_L^2} \vec{H}, \tag{1.5}$$

with

$$\lambda_L = \sqrt{\frac{m^* c^2}{4\pi n_s e^2}}. \tag{1.6}$$

The solution to this partial differential equation for a slab is simply a decaying exponential of the form $H = H' \exp(-x/\lambda_L)$. Thus one defines the first characteristic length scale of a superconductor, λ_L, the London penetration depth, which is directed along the skin depth in a metal. It is simply the characteristic length that an external magnetic field can penetrate into the bulk of a superconducting crystal before decaying away. For atomic superconductors like Pb, Hg. and Sn the penetration depth is of the order of nanometers.

Without giving a microscopic explanation of the superconducting mechanism, the London theory proved to be successful in describing the superconducting behavior and vortex states in extreme type-II superconductors, where vortices can be considered as point-like objects [20].

1.1.3 The Ginzburg-Landau theory

Ginzburg and Landau developed a phenomenological theory of superconductivity in 1950 [21]. The heart of the theory is called the order parameter, denoted here by Ψ. One may think of the order parameter as the wave-function of the charge-carriers, Cooper-pairs, in the superconductor and $|\Psi|^2$ is then the density of Cooper-pairs:

$$n_s = |\Psi|^2, \qquad (1.7)$$

where n_s is the density of the superconducting electrons. By definition, the order parameter is equal to zero above the superconducting critical temperature T_{c0} and become finite below T_{c0}.

The Ginzburg-Landau theory and its validity will be discussed in section-(1.1.5). Here, I just mention the two Ginzburg-Landau equations:

$$\alpha\Psi + \beta|\Psi|^2\Psi + \frac{1}{2m^*}(-i\hbar\vec{\nabla} - \frac{2e}{c}\vec{A})^2\Psi = 0, \qquad (1.8)$$

$$\vec{j}_s = -\frac{i\hbar e}{m^*}(\Psi^*\vec{\nabla}\Psi - \Psi\vec{\nabla}\Psi^*) - \frac{4e^2}{m^*c}|\Psi|^2\vec{A}, \qquad (1.9)$$

where the superconducting current density, $\vec{j}_s$, is given by the Maxwell equation

$$\vec{j}_s = \frac{c}{4\pi}rotrot\vec{A}. \qquad (1.10)$$

With this theory it becomes possible to describe spatial distribution of superconducting electrons, taking into account the finite size of the vortex core. This was impossible within the framework of the London theory.

1.1.4   The BCS theory

In 1957, the microscopic mechanism of superconductivity was described by Bardeen, Cooper and Schrieffer [23]. The formalism of this microscopic theory is much more complicated then the one of the Ginzburg-Landau theory which will be used in this thesis. The vortex structure and the critical parameters can be precisely calculated using Ginzburg-Landau theory and the microscopic level

is not necessary at all for the purpose of this thesis. Therefore, the discussion of the BCS theory will be limited to the basics.

The BCS theory makes a crucial assumption at the beginning: that an attractive force exists between electrons, which can overcome the Coulomb repulsion. In many superconductors the attractive interaction between electrons (necessary for pairing) is brought about indirectly by the interaction between the electrons and the vibrating crystal lattice (the phonons). Roughly speaking, the picture is the following: An electron moving through a conductor will cause a slight increase in concentration of positive charges in the lattice around it; this increment in turn can attract another electron. In effect, the two electrons are then held together with a certain binding energy. If this binding energy is higher than the energy provided by kicks from oscillating atoms in the conductor (which is true at low temperature), then the electron pair will stick together and resist all kicks, thus not experiencing resistance. However the results of BCS theory do not depend on the origin of the attractive interaction. Note that the original results of BCS were describing an **s-wave** superconducting state [5], which is the rule among low-temperature superconductors but is not realized in many *unconventional superconductors*, such as the **d-wave** high-temperature superconductors. Extensions of BCS theory exist to describe these other cases, although they are insufficient to completely describe the observed features of high-temperature superconductivity.

Therefore, BCS theory gives an approximation for the quantum-mechanical state of the system of (attractively interacting) electrons inside the metal. This state is known as the *BCS state*. Whereas in the normal metal electrons move independently, in the BCS state they are bound into *Cooper pairs* by the attractive interaction [28].

1.1.5   The Ginzburg-Landau theory and the general boundary condition

Ginzburg-Landau (GL) theory is based on an expansion of the free energy in powers of the order parameter, which is small close to the superconducting/normal transition at the critical temperature T_c. In this way, it is immediately clear that the GL theory is in principle valid only near T_c.

Here the main principles of the GL theory will be described and will be derived the well known Ginzburg-Landau equations. The standard notation is being used (see for example, textbooks [29, 31]), where $\vec{H}(\vec{r})$ denotes the local value of the magnetic field, related to the vector potential as $\mathrm{rot}\,\vec{A}(\vec{r})$. The magnetic induction $\vec{B}$ can be found as the averaged value of $\vec{H}$ over microscopic lengths and will be written as $\langle \vec{H} \rangle$. The applied field (in general, inhomogeneous) will be denoted by $\vec{H}_0(\vec{r})$.

The GL-functional for the free energy: Near T_c the Gibbs free energy of a superconductor can be expressed as [31]

$$G_{sH_0} - G_{nH_0} = \int \left(\alpha|\Psi|^2 + \frac{1}{2}\beta|\Psi|^4 + \frac{1}{2m^*}\left|\left(-i\hbar\vec{\nabla} - \frac{e^*}{c}\vec{A}\right)\Psi\right|^2 - \frac{(\vec{H} - \vec{H}_0)^2}{4\pi} \right) dV_s,$$

$$(1.11)$$

where H is the local microscopic field at a given point of the superconductor and $G_{sH_0} - G_{sH_0}$ is the difference between the free energy of the sample in the superconducting state and the normal state in applied magnetic field H_0. The integration is performed over the volume of the superconductor V_s.

Every part of the integrand in Eq. (1.11) describes some physical property. In principle, it is possible to introduce some extra terms in the energy functional in order to describe the superconducting state deeper in the superconducting phase [34], but the achieved corrections are very small and rarely considered.

The first part of Eq. (1.11) is the expansion of the free energy density for a homogenous superconductor in the absence of an external magnetic field in power of $|\Psi|^2$ near the zero-field critical temperature $T_{c0} \equiv T_c(H_0 = 0)$,

$$\alpha|\Psi|^2 + \frac{1}{2}\beta|\Psi|^4, \qquad (1.12)$$

where α and β are some phenomenological expansion coefficients which are characteristics of the material. The coefficient α is

negative and changes sign as temperature is increased over T_{c0} ($\alpha \propto (T - T_{c0})$), while β is a positive constant, independent of temperature. By minimizing expression (1.12) one can extract the Cooper-pair density corresponding to the energy minimum at temperatures below T_{c0} as

$$|\Psi_0|^2 = -\frac{\alpha}{\beta}. \qquad (1.13)$$

The next term in the integrand of Eq. (1.11) is clearly the kinetic energy of Cooper-pairs:

$$\frac{1}{2m^*}\left|(-i\hbar\vec{\nabla} - \frac{e^*}{c}\vec{A})\Psi\right|^2, \qquad (1.14)$$

where the mass of a Cooper-pair m^* is two times the mass of an electron m, and the charge of the Cooper-pair e^* is two times the charge of the electron e. It describes the energy cost when the superconducting density is non-homogenous.

The last term in Eq. (1.11)

$$-\frac{(\vec{H} - \vec{H}_0)^2}{4\pi}dV_s, \qquad (1.15)$$

describes the magnetic energy of the magnetic field of the super-currents, which measures the response of the superconductor to an external field and is nothing else than the difference between the local and applied magnetic field. Note that for a superconductor in an external field, the equilibrium state is not defined by the Helmholtz free energy but the Gibbs free energy which are actually calculated in Eq. (1.11). The difference lies in the energy of the magnetic field in the presence of a superconductor.

Note that $G_{sH_0} - G_{nH_0}$ is a function of $\Psi(\vec{r})$ and $\vec{A}(\vec{r})$. By minimizing the free energy, given by the functional Eq. (1.11), with respect to small variations in Ψ and $\vec{A}$, respectively, a set of coupled differential equations (so called GL equations) is obtained [5, 31],

$$\alpha\Psi + \beta|\Psi|^2\Psi + \frac{1}{2m^*}(-i\hbar\nabla - 2e\vec{A})^2\Psi = 0 \qquad (1.16)$$

$$\vec{j} = \nabla \times \vec{h} = \frac{e}{m^*}\left[\Psi^*\left(-i\hbar\nabla - 2e\vec{A}\right)\Psi + \Psi\left(-i\hbar\nabla - 2e\vec{A}\right)\Psi^*\right]$$
$$(1.17)$$

where $\vec{j}$ is supercurrent density. The GL equations provide a complete information about the superconducting state: $\Psi(\vec{r})$ gives the spatial distribution of the Cooper pair density, taking into account a possible variation in their concentration, whereas $\vec{A}(\vec{r})$ describes the local distribution of the magnetic field within the superconductor. Eq. (1.16) and (1.17) are not mutually independent and have to be solved self-consistently.

Boundary conditions: When minimizing Eq. (1.11) with respect to a variation in the order parameter $\Psi^* + \partial\Psi^*$, the following expression is obtained in addition to the first GL equation (see Ref. [32])

$$\frac{i\hbar}{2m^*}\int \vec{n} \cdot \partial\Psi^*(-i\hbar\vec{\nabla} - 2e\vec{A})\Psi dS = 0. \qquad (1.18)$$

where the integration is performed over the surface of a superconductor and $\vec{n}$ is the unit vector normal to the surface of the superconductor. As Eq. (1.18) has to be satisfied for an arbitrary function $\partial\Psi^*$, it is clear that at the boundary of a superconductor

$$\vec{n} \cdot (-i\hbar\vec{\nabla} - 2e\vec{A})\Psi = 0 \qquad (1.19)$$

Eq. (1.19) physically means that no supercurrent can flow perpendicularly through the sample boundary. In the case of finite
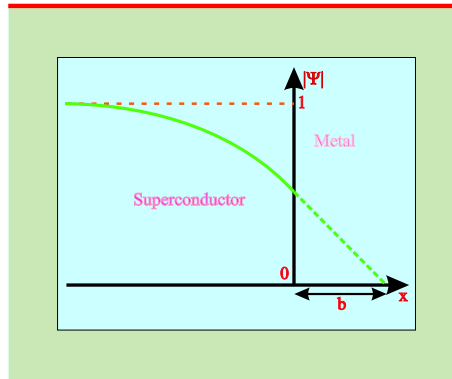
Fig. 1.4 The superconducting-normal metal interface: the illustration of the spatial dependance of the superconducting order parameter $|\Psi|$ where b denotes the extrapolation length [29].

superconducting samples such a boundary condition has a profound influence on the nucleation process and geometry of the superconducting state.

For a superconductor-normal metal interface Eq. (1.18) (and consequently the boundary condition) must be modified due to exchange of electrons (proximity effect) between two materials. De Gennes [29] has generalized the expression (1.19) to

$$\vec{n}(-i\hbar\vec{\nabla} - 2e\vec{A})\Psi \Big|_{boundary} = \frac{i}{b}\Psi \Big|_{boundary} \qquad (1.20)$$

The quantity b (real number) is called the extrapolation length, and has been introduced to account for a finite length over which the order parameter penetrates into a normal metal (see Fig. 1.4). The exact numerical value of b is predominantly determined by the character of the interface, i.e., for superconductor in contact with :
   * vacuum or an insulator: $b \to \infty$
   * normal metals: $b > 0$, and for ferromagnets: $b \to 0$,
   * a superconducting layer with a higher T_c: $b < 0$.

1.1.5.1 **Characteristic length scales**   The GL theory introduces two important characteristic length scales: the coherence length $\xi(T)$

and the penetration depth $\lambda(T)$ (Fig. (1.5)). $\lambda(T)$ and $\xi(T)$ can be derived from the first and second Ginzburg-Landau equation respectively.

Penetration depth λ: The typical length scale over which the magnetic field $\vec{H}$ varies is the penetration depth $\lambda(T)$.

If we consider a superconductor in a weak magnetic field with the sample dimensions much larger than the magnetic penetration depth, in a first order approximation, the value of Cooper-pair density can be replaced by its equilibrium zero-field value

$$|\Psi| = \Psi_0 = \sqrt{-\frac{\alpha}{\beta}}. \tag{1.21}$$

Eq. (1.9), after taking curl of both sides, now becomes

$$rot\vec{j}_s = -\frac{4e^2}{m^*c}|\Psi|^2 rot\vec{A}, \tag{1.22}$$

Using Eq. (1.4) and Maxwell equation, and taking into account that $\alpha < 0$, this can be rewritten as,

$$\vec{H} + \frac{m^*c^2\beta}{16\pi e^2|\alpha|}rotrot\vec{H} \tag{1.23}$$

and the characteristic length scale over which the magnetic field $\vec{H}$ can vary is given by,

$$\lambda(T) = \sqrt{\frac{m^*c^2}{16\pi e^2|\Psi_0|^2}} = \sqrt{\frac{m^*c^2}{8\pi e^2 n_s}} = \sqrt{\frac{m^*c^2\beta}{16\pi e^2|\alpha|}}, \tag{1.24}$$

where the density of superconducting electrons $n_s = 2|\Psi_0|^2 = 2|\alpha|/\beta$ and the mass of a Cooper-pair is two times the electron mass $m^* = 2m$.
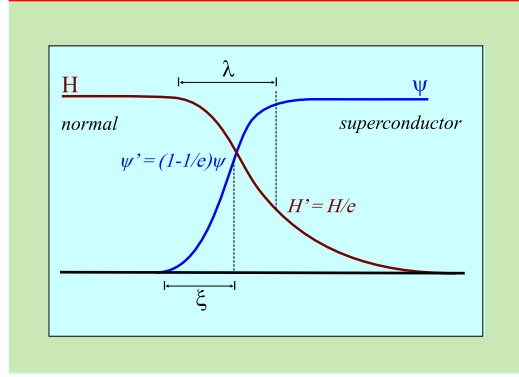
Fig. 1.5   The spatial distribution of the order parameter Ψ and the magnetic field H at the superconducting/normal surface boundary [30].

From Eq. (1.24) it follows that the penetration depth $\lambda(T)$ varies as a function of temperature as

$$\lambda(T) \propto (1 - T/T_{c0})^{-1/2}, \qquad (1.25)$$

Since $|\Psi_0| \propto |\alpha| \propto (T_{c0} - T)$, the relation between the temperature dependent penetration depth $\lambda(T)$ and the London penetration depth $\lambda_L(0)$ at absolute zero temperature may differ for pure and dirty materials [30]:
when $l_{el} \gg \xi_0$(pure),

$$\lambda(T) = \frac{\lambda_L(0)}{\sqrt{2}}(1 - T/T_{c0})^{-1/2}, \qquad (1.26)$$

and when $l_{el} \ll \xi_0$ (dirty)

$$\lambda(T) = \frac{\lambda_L(0)}{\sqrt{\frac{\xi_0}{1.33 l_{el}}}}(1 - T/T_{c0})^{-1/2}, \qquad (1.27)$$

here l_{el} denotes the elastic mean free path.

The coherence length ξ: The coherence length $\xi(T)$ indicates the typical length scale over which the order parameter can vary. Let us now consider a second example where Ψ varies only in the z-direction, but the applied magnetic field is zero. In this case, the first GL equation is one dimensional,

$$\alpha\Psi + \beta|\Psi|^3 - \frac{\hbar^2}{2m^*}\frac{d^2}{dx^2}\Psi = 0. \tag{1.28}$$

Assuming Ψ is real, we can introduce a dimensionless order parameter

$$\Psi_0 = f\Psi_0, \tag{1.29}$$

where Ψ_0, corresponds to the state with lowest free energy when $\alpha < 0$, given by Eq. (1.21). Thus Eq.(1.28) becomes

$$-\frac{\hbar^2}{2m^*|\alpha|}\frac{d^2 f}{dz^2} - f + f^3 = 0. \tag{1.30}$$

A natural length scale for spatial variations of the order parameter is therefore

$$\xi(T) = \sqrt{\frac{\hbar^2}{2m^*|\alpha|}}, \tag{1.31}$$

which is known as the GL coherence length. Since α depends on temperature as $\alpha \propto (T - T_{c0})$, the coherence length varies as a function of temperature as

$$\xi(T) \propto (1 - T/T_{c0})^{-1/2}, \tag{1.32}$$

or for pure and dirty materials [30]:

when $l_{el} \gg \xi_0$(pure),

$$\xi(T) = 0.74\xi_0(1 - T/T_{c0})^{-1/2}, \qquad (1.33)$$

and when $l_{el} \ll \xi_0$ (dirty)

$$\xi(T) = 0.855\sqrt{\xi_0 l_{el}}(1 - T/T_{c0})^{-1/2}. \qquad (1.34)$$

1.1.6   Type-I and Type-II superconductors

The value of the Ginzburg-Landau parameter $\kappa = \lambda(\text{T})/\xi(\text{T})$ determines the behavior of a bulk superconductor in an applied magnetic field H_0. Depending on the value of κ (being smaller or larger than $1/\sqrt{2} \simeq 0.71$) a distinction can be made between type-I and type-II superconductors. When $\kappa < 1/\sqrt{2}$ the sample is a type-I superconductor, on the other hand, if $\kappa > 1/\sqrt{2}$ then the sample is type-II superconductor.

All superconducting elements except niobium are type-I superconductors. Besides niobium, all superconducting alloys, chemical compounds and the high-T_c superconductors belong to the second group. One should note that this rigid distinction holds only for bulk superconductors (see Fig. 1.6). In mesoscopic samples, the behavior of the superconductor depends not only on κ but on the geometrical parameters as well [1, 5, 9, 14, 32].

Bulk samples with $\kappa < 0.42$ are pure type-I superconductors. For fields below the thermodynamical critical field $\vec{H}$ the superconductor is in a Meissner state and all flux is expelled from the sample. At the critical field the magnetic field penetrates the sample, superconductivity is destroyed and the sample becomes normal. For $0.42 < \kappa < 1/\sqrt{2} \simeq 0.71$ we still consider the superconductor to be of type-I kind, although the Meissner state does not change immediately into the normal state with increasing field. At the field $\vec{H}_c$ flux can penetrate the inner part of the sample, while near the surface of the sample, a layer remains superconducting (so-called *surface superconductivity*). For fields
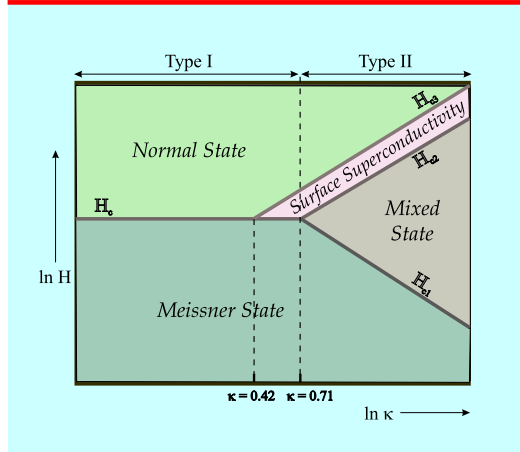
Fig. 1.6 the dependence of the characteristics of bulk superconductors on the value of the Ginzburg-Landau parameter κ. H_c and $H_{ci}|_{i=1-3}$ are explained in the text and denote the critical fields determining regions with different behaviour of the superconductor [36].

higher than the surface critical field $\vec{H}_{c3}$ the whole sample is in the normal state.

On the other hand, type-II superconductors ($\kappa > 0.71$) have remarkably different behavior. An external magnetic field (H_0) between the lower and upper critical fields (H_{c1} and H_{c2}, respectively) of a type-II superconductor does not penetrate uniformly through the sample. Rather, the magnetic field inside the sample becomes "quantized" in units of the flux quantum $\phi_0 = hc/2e$ into arrays of magnetic flux tubes. These are called *vortices*. In 1957, Abrikosov found that these vortices construct a triangular lattice inside the superconductor; each flux line contains a flux quantum, and is surrounded by currents which partially screens the magnetic interaction with neighboring flux lines, thereby lowering the free energy of the superconductor. Consequently, the "vortex state" enables type-II superconductors to sustain high magnetic fields and large applied current densities. Such a situation holds for $H_{c1} < H_0 < H_{c2}$ where H_{c2} is the so-called upper critical field, much larger than H_c. Such a magnetic field range with partial field penetration in the superconductor has been discovered by Shubnikov (1937) and is called the *Shubnikov phase*. Other names for
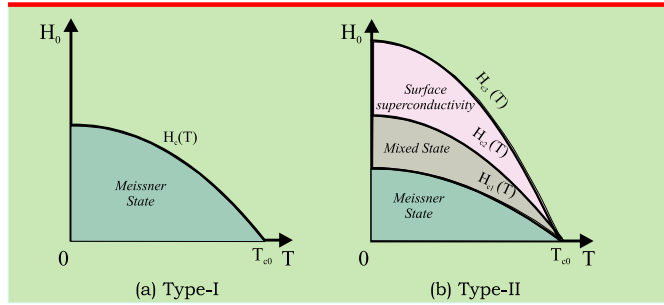
Fig. 1.7 $H - T$ phase diagram for type-I (a) and a type-II (b) bulk superconductor.

this field and temperature range (see Fig. 1.7) are the *Abrikosov vortex state*, and *the mixed state.*

At $H_0 > H_{c2}$ a macroscopic sample does not repel the flux, and $B \equiv H$. At the same time, at $H_{c2} < H_0 < H_{c3}$ a thin surface superconducting layer still exists (for bulk superconductors $H_{c3} = 1.69 H_{c2}$). After the H_{c3} field is exceeded, superconductivity is destroyed and the entire sample is in the normal state.

The critical fields H_c, H_{c1}, H_{c2} and H_{c3} depend on temperature. The H-T phase diagrams for both type-I and type-II superconductivity are shown in Fig. 1.7. Both types have also a different behavior of the magnetization as a function of the external magnetic field, as shown in Fig. 1.8. The magnetization of the superconductor is defined as $\vec{M} = (\vec{B} - \vec{H}_0)/4\pi$ where $\vec{B}$ is the magnetic induction and can be obtained by averaging the local magnetic field over the sample volume ($\vec{B} = \langle \vec{H} \rangle$).

At $H_0 < H_c$ a type-I superconductor is in the Meissner state and all flux is expelled from the sample: $\langle H \rangle = 0$ and $-4\pi M = H_0$. At larger fields, the applied field penetrates into the superconductor which becomes normal: $\langle H \rangle = H_0$ and $M = 0$. Type-II superconductors are in the Meissner state at $H_0 < H_{c1}$ and $-4\pi M = H_0$. In the mixed state ($H_{c1} < H_0 < H_{c2}$) the absolute value of the magnetization $|M|$ decreases with increasing field until it vanishes at the second critical field.

The discovery of high-temperature superconducting oxides in 1986 has opened up a new era of intense research in the basic physics of superconductivity and opportunities for a broad range of device applications. High-temperature superconductors (HTS) are
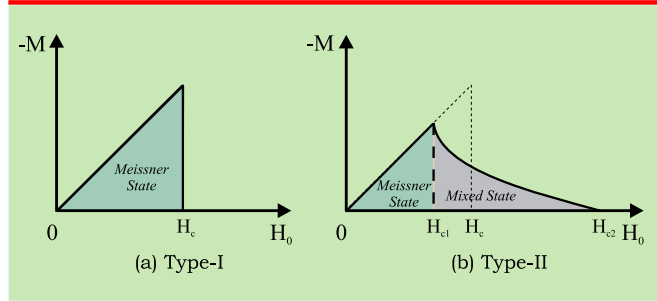
Fig. 1.8 $H - T$ phase diagram for type-I(a) and a type-II(b) bulk superconductor.

"extreme" type-II superconductors. The combination of the high transition temperatures ($T_c \sim 100$ K, compared to T_c of 1 - 10 K in conventional superconductors), short superconducting coherence lengths, long magnetic penetration depths, and large electronic anisotropies in HTS results in a "soft" vortex-solid phase which is more susceptible to large thermal and disorder fluctuations.

From the previous discussion it is evident, that superconductors have some unique material properties. However, the Ginzburg-Landau theory is only a phenomenological theory, and it does not allow for a direct calculation of the parameters for different super-conductors. Many explicit formulas for the important parameters were given above, but they usually contain the phenomenological constants α and/or β. These two constants are not a priori known and the theory provides no means of calculating them. For this, a microscopic theory is needed. However these parameters may be

Low T_c Material	T_c / K	ξ / nm		λ / nm		H_{c2} / T	
Nb	9.25	40		85		0.198	
Pb	7.2	90		40		0.08	
NbTi	9.5	4		300		13	
PbBi	8.3	20		200		0.5	
High T_c Material	**T_c / K**	ξ_{ab} / nm	ξ_c / nm	λ / nm	λ / nm	$H_{c2\perp}$ / T	$H_{c2\parallel}$ / T
$Bi_2Sr_2CaCu_2O_{8+\delta}$	94	2	0.1	200-300	15-150	> 60	> 250
$YBa_2Cu_3O_{7-\delta}$	93	1.6	0.3	150	0.8	110	240

Table 1.1 Upper critical temperature, superconducting coherence length and London penetration depth in different low T_c (LTS) and High T_c (HTS) superconductors [33].

determined by experiment. A list of physical properties of some common superconductors is provided in Table. 1.1.

It is easy to spot the difference between the low T_c and high T_c superconductors in Table-1.1. Thus extreme type-II (HTS) superconductors posses large GL parameters κ (i.e. $\lambda \gg \xi$), large upper critical fields $H_{c2}(T)$, and small lower critical fields H_{c1}(T). The high T_c materials in the table are very anisotropic. It means that direction plays a role in the compound and, for example, the coherence length is different when measured in different directions. The subscript ab refers to the parameter in the CuO-plane while subscript c is perpendicular to the CuO-plane for the two high T_c superconductors BSCCO and YBCO. It should be noted, that also some low T_c materials posses anisotropy. Nb is for example slightly anisotropic.

1.2 MESOSCOPIC SUPERCONDUCTIVITY

The Greek word meso means "in between". Mesoscopic physics refers to the physics of structures of intermediate sizes, ranging from a few atomic radii to a few microns. In case of superconductors, samples are called mesoscopic when their sizes are comparable to the coherence length ξ and the magnetic penetration depth λ. The recent progress in micro/nanofabrication technologies makes it possible to study the properties of superconductors in mesoscopic scale and nowadays it receives immense attention.

1.2.1   Properties of mesoscopic superconductors

Today's nanotechnology can provide valuable insight into the nature of mesoscopic superconductors, whose linear dimensions can be comparable to the coherence length or the inter-vortex distance of the Abrikosov lattice. In mesoscopic superconductors the properties are largely influenced by confinement effects [5]. The boundary conditions imposed by the sample shape on a superconductor strongly influences the nucleation of the superconducting state, which makes the behavior of the mesoscopic samples significantly different from a bulk sample.

For example, the value of the Ginzburg-Landau parameter $\kappa = \lambda(T)/\xi(T)$ determines the behavior of a bulk superconductor in an applied magnetic field H_0 (see section-1.1.6). Depending on the value of κ (being smaller or larger than $1/\sqrt{2} \simeq 0.71$) a distinction can be made between type-I and type-II superconductors. But in case of mesoscopic samples, the behavior of the superconductor depends not only on GL parameter κ but on the geometrical parameters as well. In thin superconducting films the distinction between type-I and type-II superconductivity depend on both κ, and the sample thickness d. Since the effective London penetration depth, defined as $\Lambda = \lambda^2/d$, increases considerably in films with thickness $d \ll \lambda$, the vortex state can appear in thin films made of material with $\kappa < 1/\sqrt{2}$ (thus is bulk type-I). Therefore, in case of mesoscopic superconductor, one can introduce the effective Ginzburg- Landau parameter $\kappa^* = \Lambda/\xi$ which defines the type of superconductivity as type-I when $\kappa^* < 1/\sqrt{2}$ and type-II when $\kappa^* > 1/\sqrt{2}$.

In 2D-confined mesoscopic samples the distinction between type-I and type-II superconductors is determined by κ, thickness d and also by the lateral dimensions of the sample [14]. Because of the small sample size, the vortex configuration in such disks is different from the triangular Abrikosov lattice, the lowest energy configuration in bulk type-II superconductors. The competition between the vortex-vortex interaction and the boundary that tries to impose its symmetry determines the (meta) stable vortex configurations [9]. Recently Cabral *et. al* [49] showed that a large circular disk will favor vortices situated on a ring near the boundary and only far away from the boundary its influence diminishes and the triangular lattice may reappear. The large variety of vortex matter in mesoscopic samples was observed depending on the geometry, the size, the applied field and the temperature. For example, giant-vortex states, multi-vortex states or a combination of them.

1.2.1.1 **Multi- and giant- vortex state:**   Superconducting vortices are topological singularities in the order parameter. In a bulk system, each vortex carries a single flux quantum ($\Phi_0 = ch/2e$), whereas vortices with multiple flux quanta are not favorable energetically. In small superconductors, however, the situation may

be different. The vortex configuration in mesoscopic superconductor is strongly affected not only by vortex-vortex interaction but also by the boundary, leading to corruption of the Abrikosov triangular lattice and formation of two kinds of fundamentally new vortex states; (i) *multivortex states* with a spatial arrangement of singly quantized vortices, and (ii) *giant vortex states* with a single, multiply quantized vortex in the center.

In the *multivortex state*, the flux penetrates the mesoscopic sample at several positions where individual vortices are created. In this respect, the multivortex state in mesoscopic confined samples is the analogue of the Abrikosov vortex state in bulk superconductors, i.e, the finite-size version of Abrikosov lattice. These vortices are defined by the separate zeros of the Cooper-pair density, with a superconducting phase change of 2π around each of them (see Fig. 1.9(a,c)). Vortex cores may deform close to each other and overlap. For a sufficiently small sample, several vortices can overlap so strongly that it become energetically more favorable to form a *giant vortex*, where single vortices combine into one big vortex, with a corresponding single minimum in the Cooper-pair density and a multiple 2π phase change around it [1]. Experimentally, a direct experimental proof for the existence of these two distinct vortex states in mesoscopic disks has been offered recently by Kanda *et al.* [53]. They developed the multiple-small-tunnel-junction (MSTJ) method, in which several small tunnel junctions with high tunnel resistance are attached to a mesoscopic superconductor in order to detect small changes in the local density of states (LDOS) under the junctions. In this way it became possible to monitor experimentally the continuous transition from the multivortex state to the giant vortex state and transitions between different multivortex states with the same total number of vortices [53].

The behaviour of mesoscopic superconductors has attracted much interest, especially since the prediction of this two fundamentally different states of vortices in them expected over most of the magnetic field range below the second critical field H_{c2}. This has prompted a large number of numerical and experimental studies that continue to bring surprises: the symmetry-induced antivortices [40], paramagnetic Meissner effect [52], first evidence for giant vortex states [53], multiple phase transitions within the supercon-
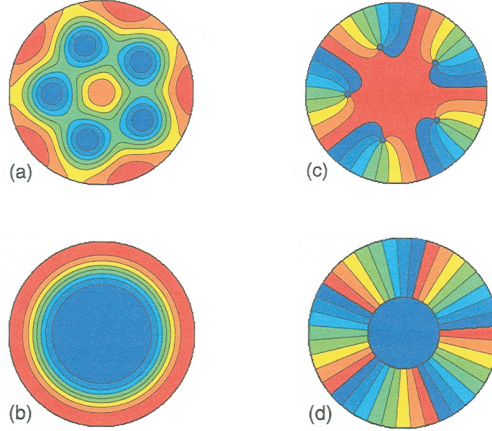
Fig. 1.9 The Cooper-pair density for the multivortex state (a) and the giant vortex state (b), and the phase of the order parameter for the multivortex state (c) and the giant vortex state (d) with vorticity $L = 5$ in a superconducting disk with radius R/ξ =6.0. High (low) Cooper-pair density is given by red (blue) regions. Phases near 2π (0) are given by red (blue) [46].

ducting state [54], negative and fractional vortices [55] are just some of the examples.

1.2.1.2 **Vorticity:** A single quantity characterizing a vortex state was introduced as *vorticity L* [1]. In multivortex states, the vorticity is nothing else than the number of vortices i.e., number of zeros of the order parameter. But in case of giant vortex state one has to look at the phase of order parameter along a closed path around the vortex. Vorticity L are then given by the multiplicity of phase by 2π. Fig. 1.9(c) shows the contour plot of the phase of the order parameter for the multivortex state of Fig. 1.9(a). Blue color indicates phases near zero and red phases near 2π. By going around near the boundary of the disk, the phase changes 5 times with 2π. This means that the total vorticity of the disk is L=5. By going around one single vortex the phase changes only by 2π. In Fig. 1.9(d) the phase of the order parameter is shown for the giant vortex configuration of Fig. 1.9(b). By going around the giant vortex, the phase of the order parameter changes 5 times with 2π, which means that the giant vortex state alone has vorticity L=5.
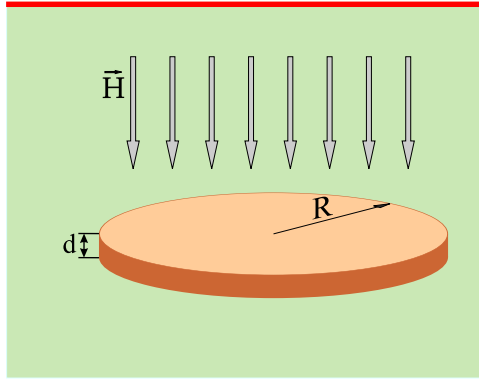
Fig. 1.10   Oblique view of the considered system: a superconducting disk of radius R and thickness d in presence of homogeneous, perpendicular, applied magnetic field $\vec{H}$.

However, the determination of vorticity is not straight forward in case of an inhomogeneous applied magnetic field (like for superconductor in the field of a neighboring ferromagnet). Although the rule of the 2π-change of phase around the vortex still applies, the vorticity of a multivortex does not always corresponds to the number of zeroes in the order parameter distribution. As the field is inhomogeneous, vortices with opposite polarity may appear (so-called antivortices, with phase change of 2π in opposite direction (and therefore individual vorticity L = -1) leading to the decrease of the total vorticity [5].

1.2.2   Submicron superconducting disk in homogeneous magnetic field

In this chapter the basic features of the superconductive state in superconducting disks with radii of few coherence lengths ξ will be presented. The main intention for this presentation is to be familiar with behavior of a superconducting disk in homogeneous perpendicular magnetic field (Fig. 1.10). We will refer later this result, when inhomogeneous field is applied which is the main scope of this thesis.

The theoretical analysis is based on a full self-consistant numerical solution of the the Ginzberg-Landau equations, following the approach used by Schweigert and Peeters [1]. To understand the underlying physics, the Cooper-pair density $|\Psi|^2$, current and
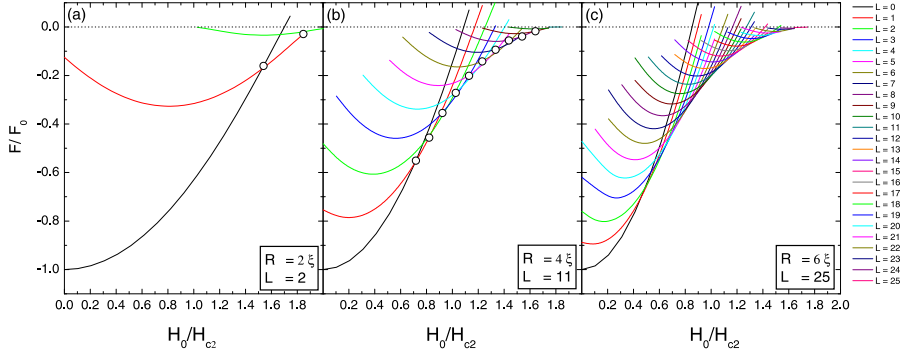
Fig. 1.11 The free energy as a function of the applied magnetic field for cylindrical disks with thickness $d/\xi = 5.0$, and radius $R/\xi = 2.0$ (a), 4.0 (b) and 6.0 (c) respectively, for different vortex state L.

magnetic field distributions in the disk in homogeneous applied magnetic field H_0 have been calculated.

Fig. 1.11 shows Gibbs free energy for different radius of the superconducting disk in increasing applied magnetic field. Here the thickness of all disks is fixed ($d = 0.5\xi$) and the Ginzburg-Landau parameter equals $\kappa = 0.28$, with disks of radii $R/\xi = 2.0$, 4.0 and 6.0. With increasing the radius of the disk the transition between the superconducting state and the normal state ($F = 0$ in Fig. 1.11) occurs at lower applied magnetic field. This transition was found at magnetic field H_0/H_{c2}= 2.02, 1.82 and 1.65 for R/ξ =2, 4 and 6, respectively.

One should also note the increase of maximul vorticity for large superconducting disks. For example, we found that maximul value for L is 2, 11 and 25 for radius $R/\xi = 2.0$, 4.0 and 6.0, respectively. The transitions between different vortex states in the ground state are marked by open dots.

In Fig. 1.11, the complete energy curves for different vorticity are shown, including the metastable states (stable states with energy higher then the ground state). One can see in Fig. 1.11(a), that the vorticity of the ground state is L = 0 up to the first transition field $H_0/H_{c2} = 1.56$, so here the vorticity of the ground state changes from L = 0 to L = 1. In case of the cylinder for $R/\xi = 4.0$, the first transition from L = 0 to L = 1 state happens at H_0/H_{c2} = 0.65 which is lower than the field for $R/\xi = 2.0$ (Fig. 1.11(a)

and (b)), and in case of $R/\xi = 6.0$ the field of the first transition is $H_0/H_{c2} = 0.48$ (Fig. 1.11(c)). It is interesting to comment here on the flux quantization. The associated flux through the superconductor at first transition fields equals 3.045 ϕ/ϕ_0, 5.658 ϕ/ϕ_0 and 8.140 ϕ/ϕ_0 for $R/\xi = 2.0$, 4.0 and 6.0, respectively. Note that flux entry appears *not to be quantized* and keeps this tendency with increasing vorticity. The applied flux needed for the entry of additional vortices in the ground-state is shown in Table-1.2, for considered sizes of the superconducting disks. For more details, see Refs. [46, 49]

In Fig. 1.12, we can see the radial distributions of Current density, Cooper-pair density, and magnetic field in a cylindrical superconducting disk of radius $R = 4\xi$ in homogeneous applied magnetic field H_0. Two fixed value of magnetic field was considered where for relatively low field $H_0 = 0.50H_{c2}$ no vortex can

R= 6ξ			**R= 4ξ**			**R= 2ξ**		
L	**ϕ/ϕ_0**	**$\Delta\phi$**	**L**	**ϕ/ϕ_0**	**$\Delta\phi$**	**L**	**ϕ/ϕ_0**	**$\Delta\phi$**
1	8.140	-------	1	5.658	-------	1	3.045	-------
2	9.653	1.513	2	6.741	1.083	2	3.971	0.926
3	10.981	1.328	3	7.726	0.985			
4	12.113	1.132	4	8.640	0.914			
5	13.114	1.001	5	9.509	0.869			
6	14.025	0.911	6	10.366	0.857			
7	14.945	0.92	7	11.237	0.871			
8	15.787	0.842	8	12.064	0.827			
9	16.671	0.884	9	12.935	0.871			
10	17.544	0.873	10	13.736	0.801			
11	18.412	0.868						
12	19.331	0.919						
13	20.153	0.822						
14	21.017	0.864						
15	21.923	0.906						
16	22.781	0.858						
17	23.651	0.870						
18	24.543	0.892						
19	25.436	0.893						
20	26.332	0.896						
21	27.201	0.869						
--------	---------	-------						
--------	---------	-------						

Table 1.2   Data for different value of flux ϕ/ϕ_0 transitions of vortices and flux difference $\triangle\phi$ between two successive transitions of vorticity of superconducting cylinder with $R = 6\xi$, 4ξ and 2ξ.
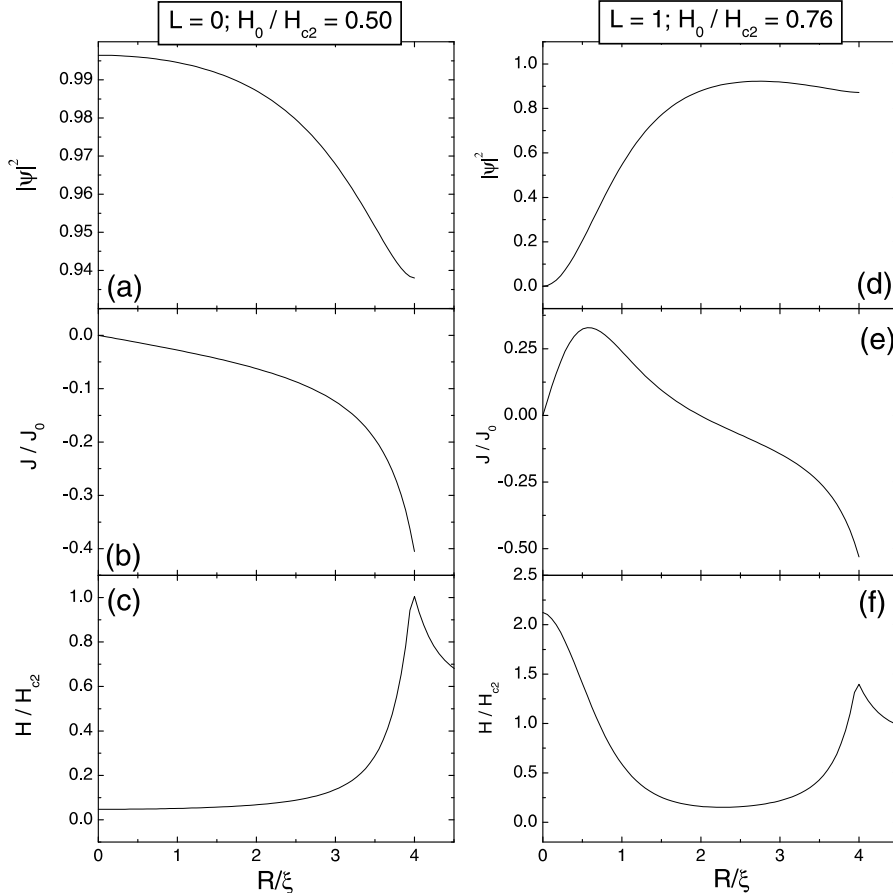
Fig. 1.12 (a, d) The Cooper-pair density, (b, e) The Current density, and (c, f)The Magnetic field distribution as a function of the radial position over the superconducting cylindrical disk with radius $R/\xi = 4$. (a, b, c) is for Meissner state, i.e, $L = 0$ with external magnetic field $H_0/H_{c2} = 0.50$ and (d, e, f) is for state $L = 1$ with external magnetic field is $H_0/H_{c2} = 0.76$.

nucleate in the disk, only the Meissner state is the stable state (see Fig. 1.11(b)) and for $H_0 = 0.76H_{c2}$ which is sufficient to create the single vortex state ($L = 1$). The value of Cooper-pair density is 1 in the superconductive region where both current and magnetic field is zero. But due to applied magnetic field, in Meissner state a circulating supercurrent is induced by the superconductor which becomes higher (see Fig. 1.12-b) at the edge to repel the applied magnetic field. From the directions of the current in the

figure, a magnetic field opposite to the applied field is seen to be generated. This results in a screening of the interior of the sample from the applied field, thus creating the Meissner effect. Fig. 1.12(c) shows the magnetic field distribution inside the superconductor for $L = 0$, the field is zero at the center of the disk and near the boundary exponentially increase out far from the disk goes to the value of applied field. A sharp peak at the edge of the disk is due to the magnetic field flux compression associating with diamagnetic supercurrent (see Fig. 1.3). We can notice that there is some minimum value of magnetic field (see Fig. 1.12-c), in what follows it will become clear that this indicates the penetration depth of the magnetic field in the flat cylinder, which leads the Cooper-pair density to become exponentially low at the edge (Fig. 1.12-a). Again with increased magnetic field when one vortex enters into the superconductor and is situated into the center of the disk, the cooper-pair density is zero in the vortex region as there is no superconductivity in this core (Fig. 1.12-d) and increases to higher value in the superconductive region over the disk and decreases slightly near the edge of the disk due to the penetration of magnetic field. The magnetic flux of applied magnetic field becomes trapped in the vortex region and since the circulating eddy currents of a vortex induce magnetic fields of their own, thus the magnetic field inside the vortex increases and become larger than the applied magnetic field (Fig. 1.12-f). At the edge it has a similar behaviour with a sharp peak as in the L = 0 situation. As in the vortex core of the disk Cooper-pair density is zero induced Meissner current also become zero. In Fig. (1.12-e) we can see a peak which results from the fact that the vortex has a magnetic field of its own due to the eddy currents which is large at the vortex edge associating with the applied magnetic field. Consequently more current is needed to balance the magnetic field at the edge of the vortex and so the sign of the paramagnetic supercurrent near the vortex is more positive. In the superconducting region the superconducting current becomes negative due to diamagnetic supercurrent. The uniform diamagnetic supercurrent is flowing along the boundary. Again the Meissner current at the edge of the disk is increased from $-0.4J_0$ to $-0.54J_0$ with increasing applied magnetic field (compare Figs. 1.12-b with 1.12-e)

From the previous discussion it is evident, that the current density, Cooper-pair density, and magnetic field in a flat cylindrical superconductor posses unique properties. In what follows in this thesis we will investigate how these basic characteristics of the superconducting state in homogeneous applied magnetic field behave in an inhomogeneous field as created by a permanent magnetic ring around the disk.

2

Introduction to magnetism

2.1 MAGNETIC MATERIALS AND HYSTERESIS

Magnetism is a force that acts at a distance and is caused by a magnetic field. This force strongly attracts ferromagnetic materials such as iron, nickel and cobalt. The basic concepts have been well understood for years. With increasing technological development magnets are being used throughout industries almost in everything from toys to computer hard disk drives. In this continuous development process it is needed to study magnetism and magnetic field behavior on a very small length scale.

Superconductivity and ferromagnetism are two of the most important collective states in solid state physics and there interaction has been studied for several decades. Since the strong internal fields in ferromagnets have a destructive action on the superconducting Cooper-pairs, ferromagnetism and superconductivity have also been considered as two antagonistic phenomena for long time. Creating artificial hybrid nanostructures composed of both superconductors(SC) and ferromagnets (FM) gives rise to a lot of new physical phenomena [5, 3, 4, 7]. In this theses we are going to explore the behavior of small superconducting disks with ferromagnetic coating.
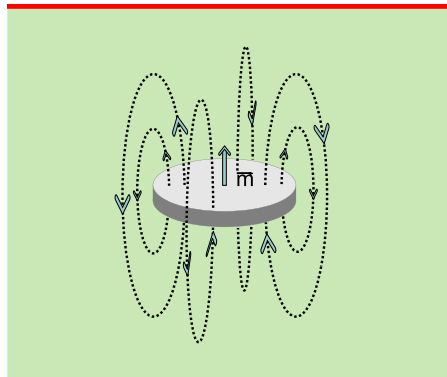
Fig. 2.1   The magnetic field lines illustrating the distribution of the magnetic field around a magnetic disk.

There are three types of magnetic materials. *Diamagnetic materials*, such as bismuth and antimony, are weakly repelled by both poles of a magnet, so they become magnetized in direction opposite to the external magnetic field. *Paramagnetic materials*, such as aluminium and platinum, react only slightly to a magnetizing force, and tend to magnetize in the direction of the external field. *Ferromagnetic material* have a non-vanishing magnetization even in the absence of an external field.

Iron, nickel, cobalt and some of the rare earths (gadolinium, dysprosium) and a wide range of alloys exhibit ferromagnetic behavior (iron or 'ferric' is the most common and most dramatic example of a ferromagnetic material). The field lines of a magnetic dipole with moment $\vec{m}$ are depicted in Fig. 2.1. The change of polarity of the field lines in the vicinity of the dipole is linked to a demagnetizing effect, which ultimately causes the material to be divided up into small sections. Thus ferromagnetic materials exhibit a long-range ordering phenomenon at the atomic level which causes the atomic magnetic moments to line up parallel with each other in a region called a domain. Within the domain, the magnetization is intense, but in a bulk sample the material will usually be demagnetized because many domains will be randomly oriented with respect to one another. In an applied magnetic field, magnetic moments tend to line up as their lowest energy state. The magnetic flux density in the material will then be increased by a
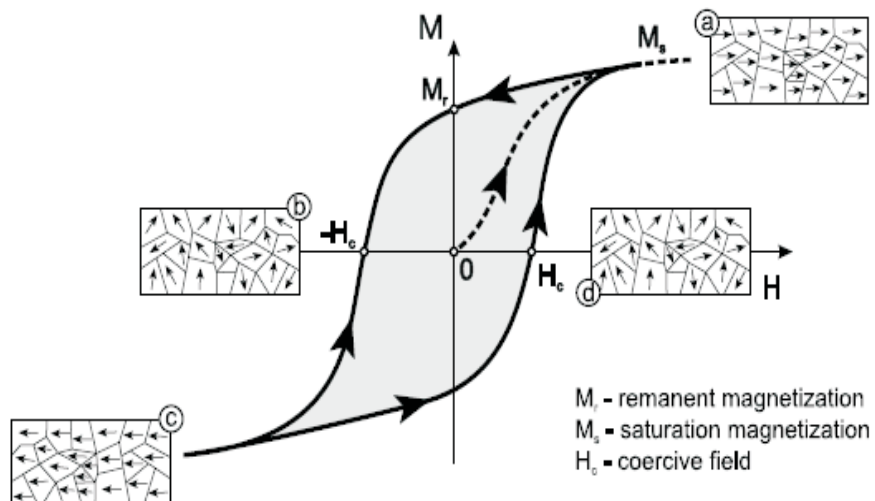
Fig. 2.2 The magnetization 'M' vs magnetic field strength 'H' for a ferromagnetic: (a) starting at zero the material follows at first a non-linear magnetization curve and reaches the saturation level, when all the magnetic domains are aligned with the direction of a field; when afterwards driving magnetic field drops to zero, the ferromagnetic material retains a considerable degree of magnetization or "remember" the previous state of magnetization; (b) at this point, when H = 0 a ferromagnet is not fully demagnetized and only the partial domain reorientation happened; (c) saturation level in the opposite direction of applied field; (d) in order to demagnetize a ferromagnetic material the strong magnetic field of the opposite direction (called "coercive field", 'H_c') has to be applied.

large factor called relative magnetic permeability of the material compared to the magnetic flux density in vacuum, $\mu_0 H$.

When the moments are aligned to the point where adding more energy would not align them any more, the material is at its maximum magnetization, or saturation magnetization. The magnetization process is not reversible, as shown by the hysteresis loop Fig. (2.2). For instance, when an external magnetic field is applied, and then reduced back to zero, there is a residual magnetization M_r left in the material. Once the magnetic domains are reoriented, it takes some energy to turn them back again. In other words, the moments tend to remain aligned to a certain extent, in a process known as remanence. The coercive force is the opposite magnetic intensity required to remove the residual magnetism. Saturation magnetization, remanence, and coercivity are three properties of

magnetic materials that are important when working on the microscopic level as well as the macroscopic level. Some compositions of ferromagnetic materials will retain an imposed magnetization indefinitely and are useful as "permanent magnets". This type of "hard" magnets are very useful in Superconductor-Ferromagnet heterostructures, as additional applied magnetic field or the field emerging from the superconductor have no effect on the magnetic state of the magnet. Throughout this thesis, only "hard" magnet will be considered. Note that all ferromagnets have a maximum temperature where the ferromagnetic property disappears as a result of thermal agitation. This temperature is called the Curie temperature and is typically higher than the working temperature of conventional superconductors.

2.2 MAGNETOSTATIC CALCULATIONS: ANALYTICAL VS. NUMERICAL APPROACH

Here we will give the basic theoretical background for the magnetostatic calculations of the stray field energy of ferromagnetic structures (for details, see Refs. [12, 8]). We start from two Maxwell-equations:

$$\vec{\nabla} \cdot \vec{B} = 0, \qquad \vec{\nabla} \times \vec{H} = \vec{j}. \tag{2.1}$$

For a "hard" ferromagnet we can take $\vec{M}(\vec{r}) \neq 0$ and $\vec{j} = 0$, so Eq.(2.1) can be rewritten as,

$$\vec{\nabla} \cdot \vec{B} = 0 = \mu_0 \vec{\nabla}.(\vec{H} + \vec{M}), \tag{2.2}$$

and consequently

$$-\vec{\nabla} \cdot \vec{H}_d = \vec{\nabla} \cdot \vec{M}. \tag{2.3}$$

Here the stray field $\vec{H}_d$ is defined as the magnetic field generated by the divergence of the magnetization. The energy contribution of the stray field is [32]

$$W_s = \frac{\mu_0}{2} \int d\vec{r} \vec{H}_d^2 = -\frac{1}{2} \int d\vec{r}' \vec{H}_d \cdot \vec{M}. \qquad (2.4)$$

The first integral is taken over all space and shows that the stray field energy is always positive, unless the stray field itself is equal to zero everywhere. The second integral in Eq. (2.4) extends over the volume of a ferromagnetic specimen. As $\vec{j} = 0$, from a Maxwell's equation

$$\vec{\nabla} \times \vec{H} = \vec{j}, \qquad (2.5)$$

thus $\vec{\nabla} \times \vec{H} = 0$, and we can define the magnetic scalar potential φ_m with,

$$\vec{H} = -\vec{\nabla}\varphi_m, \qquad (2.6)$$

and Eq. (2.3) therefore transforms into,

$$\nabla^2 \varphi_m = \vec{\nabla} \cdot \vec{M}. \qquad (2.7)$$

For a ferromagnetic cylinder with a uniform magnetization M_z along the z direction the scalar potential can be written as [12],

$$\varphi_m(\vec{r}) = -\frac{1}{4\pi} \int_v d^3r' \frac{\vec{\nabla} \cdot \vec{M}(\vec{r})}{|\vec{r} - \vec{r}'|} + \frac{1}{4\pi} \oint_s ds' \frac{\vec{n}' \cdot \vec{\nabla} \cdot \vec{M}(\vec{r}')}{|\vec{r} - \vec{r}'|}, \quad (2.8)$$

where the first integral is taken over the volume and the second over the surface of a ferromagnet. From Eq. (2.8) the stray field
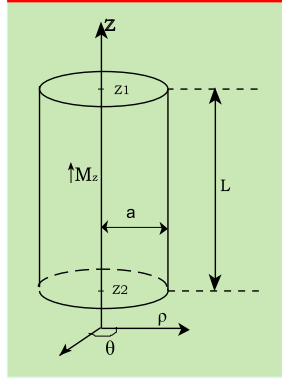
Fig. 2.3   The schematic diagram of a cylindrical magnet with magnetization along z direction, a is the radius of the cylinder and L its height.

can be calculated. If the magnetization within a ferromagnet is uniform, then Eq. (2.8), by making use of Gauss's theorem, transforms into [5, 12]

$$\varphi_m(\vec{r}) = -\frac{1}{4\pi}\vec{\nabla}_r \cdot \int d^3r' \frac{\vec{M}(\vec{r})}{|\vec{r} - \vec{r'}|}. \tag{2.9}$$

This equation gives the magnetostatic potential $\varphi_m(\vec{r})$ of an arbitrarily-shaped ferromagnet with the magnetization distribution $\vec{M}(\vec{r})$. Once $\varphi_m(\vec{r})$ is calculated, the stray field follows from Eq. (2.6).

2.2.1   Analytical approach for a magnetic cylinder:

As the ferromagnetic cylinder has a uniform magnetization, the first term of Eq. (2.8) vanishes, thus

$$\varphi_m(\vec{r}) = \frac{1}{4\pi}\oint_s ds' \frac{\vec{n'} \cdot \vec{\nabla} \cdot \vec{M}(\vec{r'})}{|\vec{r} - \vec{r'}|}, \tag{2.10}$$

$$= -\frac{1}{4\pi}\int_{s_1} \frac{M_z ds}{|\vec{r} - \vec{r'}|} + \frac{1}{4\pi}\int_{s_2} \frac{M_z ds}{|\vec{r} - \vec{r'}|}, \tag{2.11}$$

where s_1 and s_2 denote the lower and upper surface of the magnet. For a cylindrically symmetric problem a general solution can be derived as [12]:

$$\varphi_m(\mathbf{r}, \theta) = \sum_{l=0}^{\infty} \left[\mathbf{A}_l \mathbf{r}^l + \mathbf{B}_l \mathbf{r}^{-(l+1)} \right] \mathbf{P}_l cos\theta. \qquad (2.12)$$

where,

$$\varphi_m(\mathbf{r} = \mathbf{z}) = \sum_{l=0}^{\infty} \left[\mathbf{A}_l \mathbf{r}^l + \mathbf{B}_l \mathbf{r}^{-(l+1)} \right] \qquad (2.13)$$

is the solution for the problem at the symmetry axis.
The magnetic field follows from,

$$\mathbf{B}_z = -\mu_0 \frac{\partial \phi_m}{\partial z}, \qquad (2.14)$$

with the solution at the axis,

$$\mathbf{B}_z = \frac{\mu_0 m_z}{2} \left[\frac{z - z_1}{\sqrt{a^2 + (z - z_1)^2}} - \frac{z - z_2}{\sqrt{a^2 + (z - z_2)^2}} \right], \qquad (2.15)$$

in this equation, z_1, z_2 denote the coordinates of the lower and upper surface of the magnet (see Fig. 2.3). The general expression for the magnetic field is given by

$$\mathbf{B}_z = \frac{\mu_0 m_z}{2} \left[\mathbf{F}(\mathbf{r_1}, \theta_1) - \mathbf{F}(\mathbf{r_2}, \theta_2) \right], \qquad (2.16)$$

here, for $r_i \geq a$,

$$\mathbf{F}(\mathbf{r_i}, \theta_\mathbf{i}) = 1 + \sum_{n=1}^{\infty} \mathbf{P_{2n}}(0)(\frac{a}{r_i})^{2n} \mathbf{P_{2n-1}}(cos\theta_i), \qquad (2.17)$$

and, for $0 \leq r_i < a$,

$$\mathbf{F}(\mathbf{r_i}, \theta_\mathbf{i}) = \sum_{n=1}^{\infty} \mathbf{P_{2n}}(0)(\frac{r_i}{a})^{2n+1} \mathbf{P_{2n+1}}(cos\theta_i). \qquad (2.18)$$

where,

$$cos\theta_{i=1,2} = \frac{z - z_i}{\sqrt{(z - z_i^2 + \rho^2)}}, \qquad (2.19)$$

$$r_{i=1,2} = \sqrt{(z - z_i^2 + \rho^2)}. \qquad (2.20)$$

This calculation is done for a cylindrical shaped magnet. To obtain the distribution of magnetic field around of a hollow cylinder one can employ the superposition principle.

2.2.2 Numerical approach:

In the present work, to calculate at the stray field of an arbitrary shaped ferromagnet, first the magnetic field of such a ferromagnet has to be calculated numerically. Actually, it is the magnetic vector potential which appears in the Ginzburg-Landau formalism. The magnetic vector potential of a magnetic dipole is given by,

$$\vec{A} = \frac{\vec{m} \times \vec{r}}{r^2}, \qquad (2.21)$$

where $\vec{m}$ is the magnetic dipole moment, associated with the magnetic field is,

$$\vec{B} = \frac{3(\vec{m} \cdot \vec{r})r - \vec{m}r^2}{r^5}. \qquad (2.22)$$

To calculate the magnetic field of a finite size magnet, it can be derive into a set of dipoles, each of which inducing the magnetic field

$$h_z^{dipole}(x_0, y_0, z_0) = m_z \frac{2(z_0 - z_D)^2 - [(x_0 - x_D)^2 + (y_0 - y_D)^2]^2}{[(x_0 - x_D)^2 + (y_0 - y_D)^2 + (z_0 - z_D)^2]^{5/2}}, \qquad (2.23)$$

where (x_D, y_D, z_D) are the spatial coordinates of the dipole with magnetic moment m_z, and (x_0, y_0, z_0) is the point of interest for the calculation of the magnetic field. The total magnetic field is obtained after integration over the volume of the magnet:
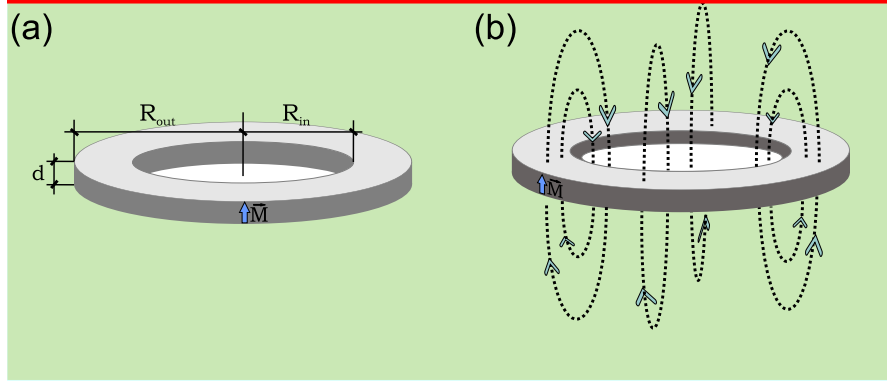
Fig. 2.4 Schematic diagram of a ring shaped magnet (a) with inner radius R_{in}, outer radius R_{out}, thickness d and (b) showing the stray field distribution inside the cavity. Magnetization $\mathbf{M}$ is along z direction

$$h_z(x_0, y_0, z_0) = \int \int \int M \frac{2(z_0 - z_D)^2 - [(x_0 - x_D)^2 + (y_0 - y_D)^2]^2}{[(x_0 - x_D)^2 + (y_0 - y_D)^2 + (z_0 - z_D)^2]^{5/2}} dx_D dy_D dz_D,$$
$$(2.24)$$

with M being the magnetization (the magnetic moment per unit volume). Note that if (x_0, y_0, z_0) is located inside the magnet, the field equals,

$$h_z^{inside}(x_0, y_0, z_0) = h_z(x_0, y_0, z_0) + \mu_0 M. \qquad (2.25)$$

Thus using this approach, we can calculate numerically the magnetic field of a magnet of any shape.

The vector potential has only the azimuthal component A_ϕ, and can be calculated analogously according to Eq. (2.21), by taking

$$A_\phi^{dipole} = \int \frac{m\sqrt{(x_0 - x_D)^2 + (y_0 - y_D)^2}}{[(x_0 - x_D)^2 + (y_0 - y_D)^2 + (z_0 - z_D)^2]^{3/2}} dx_D dy_D dz_D.$$
$$(2.26)$$

2.3 MAGNETIC FIELD: RESULTS

The aim is to explore the characteristics of a small radius superconducting cylinder with thin magnetic coating. In this paragraph,
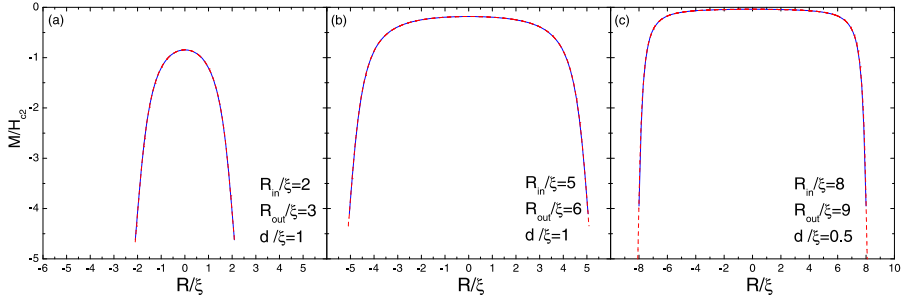
Fig. 2.5 Comparison of the analytical (red dots) and numerical (blue lines) results for stray field of magnetic cylinder of different size and thickness (see Fig. 2.4), at a distance 1ξ below the magnet.

the change of the magnetic field profile of the magnetic coating, as a function of its parameters: inner radius R_{in}, outer radius R_{out}, and the thickness d (Fig. 2.4) will be discussed in brief.

2.3.1   Ferromagnetic cylinder

For educative purposes and comparison, first we compere the analytically and magnetically calculated magnetic stray field profile.

   In Fig. (2.5) the result of magnetic field calculation is shown for both analytical and numerical approach. Cylinders of different size and thicknesses are considered and calculated the field at 1ξ below the magnet. Blue solid lines denote the numerical results, whereas red dot gives the field calculated analytically for the same set of parameters. In short, Fig. 2.5 shows perfect agreement between analytical [13] and numerical calculation.

   One should note that magnetic field changes polarity under the edge of the magnetic cylinder, with pronounced extremes close to the magnet edge. Thus extremes become smeared out for large thickness of the magnet, and/or with increasing vertical distance from the magnet.

2.3.2   The ferromagnetic ring with axial magnetization

As in this thesis we are going to investigate the shielding properties of ferromagnetic ring around a superconducting disk and main concern is taken about the field distribution inside the magnetic
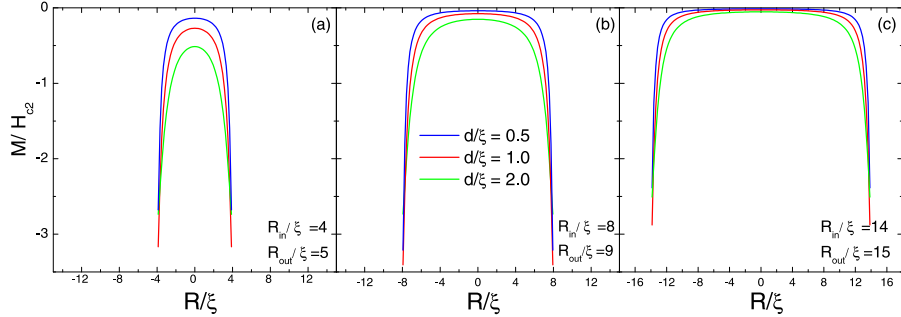
Fig. 2.6 Magnetic field distribution in the cavity of a ring magnet depends on it's inner-radius (R_{in}), outer-radius (R_{out}) and thickness d.

ring. Obviously, such a field distribution will depend on the inner and outer radius, thickness and width of the magnetic ring.

Fig. 2.6 shows the magnetic field distribution inside the magnetic ring of different sizes. The general properties of the stray field inside the magnetic ring are:

i) opposite polarity compared to the field of the corresponding magnetic cylinder (see Fig. 2.4-b),

ii) high magnetic field close to the rim of the magnetic ring, and

iii) fast decay of the magnetic field towards the center of the ring.

As shown in Fig. 2.6, thinner magnetic rings focus the stray field at the edges rather then inside the cavity (red vs. green vs. blue curve). The value of magnetic field in the center of the ring can be further reduced by increasing the inner radius of the magnet (R_{in}), as shown in Figs. 2.6(a-c).

On the other hand, increase of width of the magnetic ring (i.e, the outer radius R_{out}) *increases* the magnetic field inside the cavity, at the expense of the field at the edges (as shown in Fig. 2.7).

Therefore, by careful construction of the magnetic geometry, the resulting stray field can be fine tuned. In what follows, this property can be use to nanoengineer the properties of a superconductor in a controlled fashion.
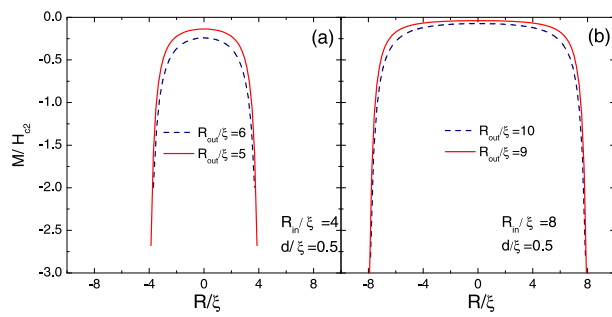
Fig. *2.7*   Magnetic field distribution in the cavity of a ring magnet depends on it's inner-radius (R_{in}), outer-radius (R_{out}), and width.

3

Superconducting disk with magnetic coating

Heterostructures on the macro- or nano-scale involving type-II superconductor and ferromagnet elements show great potential for improving superconductor properties such as critical currents and critical fields, and therefore have been extensively studied both experimentally and theoretically during the past decade. The interplay of superconductivity and ferromagnetism has been well studied theoretically and experimentally [42] for homogeneous systems. In such systems, both order parameters are homogeneous in space and suppress each other. Because Cooper pairs can leak into the normal material the critical temperature T_c of the superconductor is suppressed and signs of weak superconductivity are observed in the normal material [29]. However, by separating the superconducting (SC) and ferromagnetic (FM) subsystems in space, it is possible to avoid their mutual suppression. To avoid the proximity effect, insulating barriers are grown between the superconductor and magnetic structures [42]. If hard magnets are used, the interaction of the magnetic vortices of the superconductor with the magnetic moments of the ferromagnet may lead to an enhancement of the pinning of the vortices or to an increase of the critical fields [37]. Soft magnets, on the other hand, aid to amend superconductor performance by shielding the transport
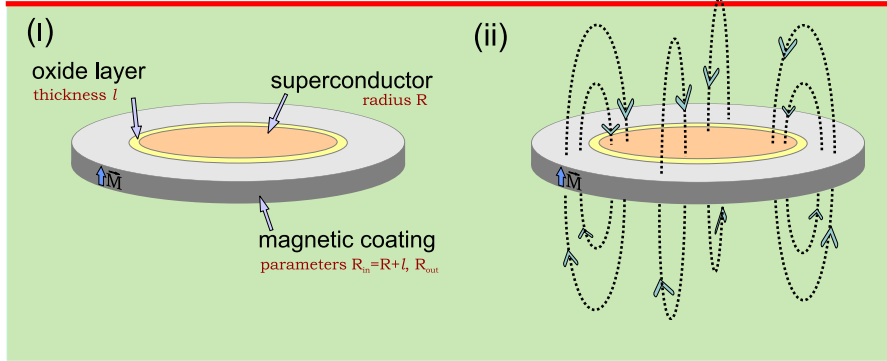
Fig. 3.1 Oblique view of the considered system: a superconducting disk of radius R and thickness d surrounded by a thin oxide layer (thickness l) and a magnetic ring (with parameters R_{in}, R_{out}, and thickness d).

current self-induced magnetic field as well as the externally imposed magnetic field [45].

In the present work we will investigate the nucleation of superconductivity in as extreme type-II superconducting disk with a ferromagnetic coating around it (see Fig. 3.1). The superconductor and ferromagnet are separated by an insulating oxide layer, typically of thickness 0.1ξ, to ensure that they are electronically decoupled.

3.1 NUMERICAL APPROACH ASSUMING CYLINDRICAL SYMMETRY

To get the distribution of both the superconducting order parameter, $\Psi(\vec{r})$, and the magnetic field (vector potential $A(\vec{r})$) the theoretical analysis is developed based on the approach used by Schweigert and Peeters [1]. A superconducting disk is considered with radius R and thickness d immersed in an insulating media exposed to an applied magnetic field.

Due to the circular symmetry of the disk cylindrical coordinates is used: ρ is the radial distance from the disk center, φ is the azimuthal angle and the z-axis is taken perpendicular to the disk plane, where the disk lies between $z = -d/2$ and $z = d/2$.

Using dimensionless variables and the London gauge, $\text{div}\vec{A}=0$, the coupled GL equations can be rewrite as,

$$(-i\vec{\nabla} - \vec{A})^2\Psi = \Psi(1 - |\Psi|^2), \tag{3.1}$$

$$-\kappa^2\Delta\vec{A} = \frac{1}{2i}(\Psi^*\vec{\nabla}\Psi - \Psi\vec{\nabla}\Psi^*) - |\Psi|^2\vec{A}, \tag{3.2}$$

with the boundary condition:

$$\vec{n} \cdot \left(-i\vec{\nabla} - \vec{A}\right)\Psi\big|_{boundary} = 0. \tag{3.3}$$

The boundary condition for the vector potential has to be taken far away from the disk

$$\vec{A}_{|\vec{r}\to\infty} = \vec{A}_0, \tag{3.4}$$

where the applied magnetic field and its vector potential are unaffected by the superconductor. Here all distances are measured in units of the coherence length $\xi = \hbar/\sqrt{-2m\alpha}$, the order parameter in $\Psi_0 = \sqrt{-\frac{\alpha}{\beta}}$, the vector potential in $c\hbar/2e\xi$, $\kappa = \lambda/\xi$ is the GL parameter, and $\lambda = c\sqrt{m/\pi/4e\Psi_0}$ is the penetration depth. We measure the magnetic field in $H_{c2} = c\hbar/2e\xi^2 = \kappa\sqrt{2}H_c$, where $H_c = \sqrt{-4\pi\alpha^2/\beta}$ is the critical field.

The free energy of the superconducting state, measured in $F_0 = H_c^2V/8\pi$ units, is determined by the expression

$$F = \frac{2}{V}\left\{\int dV\left[-|\psi|^2 + \frac{1}{2}|\psi|^4 + \left|-i\vec{\nabla}\psi - \vec{A}\psi\right|^2 + \kappa^2(\vec{h}(\vec{r}) - \vec{H}_0)^2\right]\right\}, \tag{3.5}$$

with the local magnetic field

$$\vec{h}(\vec{r}) = \vec{\nabla} \times \vec{A}(\vec{r}). \tag{3.6}$$

In this thesis, we will study an *extreme type-II* superconductor. The high-temperature superconductors are extreme type-II, with large GL parameters κ (i.e. $\lambda \gg \xi$), large upper critical fields $H_{c2}(T)$, and small lower critical fields $H_{c1}(T)$ [15]. Good example of low T_c extreme type-II superconductor is niobium di-selenide (NbSe$_2$) with superconducting transition temperature at 7.2 K, London penetration depth $\lambda_L = 265$ nm, Ginzburg-Landau Coherence length $\xi_{GL}(0) = 7.8$ nm, anisotropy $\gamma = 3$, and the upper

critical field $H_{c2} = 3.5$ T [10]. As the permanent magnetic ring will coat the superconducting disk the field strength will be higher at the edge and very low at the center, i.e., the applied magnetic field will be inhomogeneous over the disk area. We restrict ourselves to sufficiently thin disks such that $d \ll \xi, \lambda$. In this case, to a first approximation, and also due to the higher value of κ the magnetic field generated by the circulating superconducting currents can be neglected and the total magnetic field equals the applied one $\vec{H}_0$.

Within this approximation only the first GL equation is solved with $\vec{A} = \vec{A}_0$, where $\vec{H}_0 = \vec{\nabla} \times \vec{A}_0$. Therefore the Gibbs free energy is expressed by

$$F = \frac{2}{V} \int d\vec{r} |\Psi|^4, \tag{3.7}$$

with V being the volume of the sample ($V = R^2 \pi d$). it is assumed that the magnetic field has only a z-component and is uniformly distributed along the z direction. When the disk thickness becomes comparable to the penetration length, due to the Meissner effect the magnetic field is expelled from the disk. The field penetrates over a distance λ inside the disk. As a consequence, the longitudinal variation of the vector potential becomes rather strong for $d > \lambda$. Nevertheless, it was found that this does not lead to important longitudinal variations of the order parameter in disks that are thinner than the coherence length [14, 39].

The same calculation can be made for $\psi(\vec{r})$. Representing the order parameter as a series over cosines, $\Psi(z, \vec{\rho}) = \sum_k cos(k\pi z/d)\Psi_k(\vec{\rho})$, using the boundary condition Eq. (3.3) at the disk $z = \pm d/2$ and using the first GL equation (1), one can verify that the longitudinally uniform part of the order parameter Ψ_0 gives the main contribution for $(\pi\xi/d)^2 \gg 1$. Therefore, the order parameter is uniform along the z direction of the disk and we may average the first GL equation over the disk thickness. Since the order parameter does not vary in the z direction, both the superconducting current and vector potential have no z component. Then the boundary condition Eq. (3.3) is automatically fulfilled at the upper and lower sides of the disk. In case of sufficiently small radius of the sample the final vortex state should always obey the circular symmetry. Thus for a fixed value of the angular momentum L (vorticity) the order parameter is $\Psi(\vec{\rho}) = F(\rho)exp\,(iL\phi)$, and consequently both

the vector potential and the superconducting current are directed along $\vec{e}_\phi$. For a fixed angular momentum thus Eq. (3.1) reduced to a one dimensional problem:

$$-\frac{1}{\rho}\frac{\partial}{\partial\rho}\rho\frac{\partial F}{\partial\rho} + \langle(\frac{L}{\rho} - A_0)^2\rangle F = F(1 - F^2), \qquad (3.8)$$

where the vector potential is defined as, $\vec{A}_0 = \vec{e}_\phi A_0$, and the brackets $\langle\rangle$ mean averaging over the disk thickness.

The boundary conditions for the radial part of the order parameter becomes

$$\frac{\partial F}{\partial\rho}|_{\rho=r} = 0, \rho\frac{\partial F}{\partial\rho}|_{\rho=0} = 0, \qquad (3.9)$$

and correspond to zero current density at the disk surface and a finite value of the first derivative of F at the disk center. To solve Eq. (3.8) numerically, a finite-difference representation was applied on the space grid ρ_i, z_j . The steady-state solution of the GL equations is obtained using the iteration procedure

$$\eta_f F_i^k - \frac{2}{\rho_{i+1/2}^2 - \rho_{i-1/2}^2}\left(\rho_{i+1/2}\frac{F_{i+1}^k - F_i^k}{\rho_{i+1} - \rho_i} - \rho_{i-1/2}\frac{F_i^k - F_{i-1}^k}{\rho_i - \rho_{i-1}}\right)$$

$$+\langle(\frac{L}{\rho_j} - A_{j,i})^2\rangle_i F_i^k - F_i^k + 3(F_i^{k-1})^2 F_i^k = \eta_f F_i^{k-1} + 2(F_i^{k-1})^3 \quad (3.10)$$

where $A_{j,i} = A_0(z_j, \rho_i), F_i = F(\rho_i), \rho_{i+1/2} = (\rho_{j+1} + \rho_i)/2, z_{j+1/2} = (z_{j+1} + z_j)/2$; the upper index k denotes the iteration step. The introduction of the iteration parameters η_f is a well-known procedure to speed up the convergency of the iterations. It corresponds to an artificial time relaxation of the system to a steady-state with time steps $1/\eta_f$. To further improve the iteration convergency, the nonlinear term is expanded $(F_i^k)^3 = (F_i^{k-1})^3 + 3(F_i^{k-1})^2(F_i^k - F_i^{k-1})$ in the right-hand side of the first GL equation. Since the size of the simulation region exceeds by far that of the disk, a nonuniform space grid is applied to diminish the computation time. The space grid is taken uniform inside the disk, and we increased the grid spacing exponentially with distance outside the disk. This allows to use almost the same number of grid points inside and outside the disk. The calculations are performed with different number of grid points in order to check that our results are independent of the used space grid.

The nonlinear GL equations posses many steady state solutions. This fact can manifest itself in the experimental observation of hysteresis, when the measured magnetization depends whether one increases or decreases the magnetic field [1]. To mimic those real experimental conditions the calculations were performed where such that the magnetic field is slowly increased from a weak value where the disk is in the superconducting state, or to decrease the field from a large value, where the disk is in the normal state. As an example the latter case is considered. When the magnetic field is reduced below the critical value H_{nuc}, which depends on the value of the angular momentum and the disk radius, the normal state becomes unstable and transforms to a superconducting one. The critical magnetic field is obtained from the linearized first GL equation

$$\hat{L}F = 0, \hat{L} = -\frac{1}{\rho}\frac{\partial}{\partial\rho}\rho\frac{\partial}{\partial\rho} + (L/\rho - A_0)^2 - 1. \qquad (3.11)$$

The superconducting state starts to develop when the minimal eigenvalue of the operator $\hat{L}$ becomes negative. For the zero angular momentum state, the normal state transforms to the superconducting state with decreasing magnetic field below the nucleation field H_{nuc}. For nonzero angular momentum, the superconducting state appears when we cross either the lower $H_{nuc,l}$ or the upper $H_{nuc,u}$ critical magnetic fields that depends on the disk radius.

Since the order parameter is represented on a space grid, the eigenfunctions and eigenvalues of the operator $\hat{L}$ is found numerically using the Housholder technique. Starting from the critical magnetic fields $H_{nuc,l}$ or $H_{nuc,u}$, the initial order parameter is taken to be equal to the lowest eigenfunction. To avoid artificial nonlinear effects that could be produced by the initial condition, a small amplitude for this eigenfunction is taken. The initial vector potential is taken equal to the undisturbed magnetic field configuration. After finding a steady state, the applied field is reduced by a small value and a new solution is searched. Decreasing slowly the magnetic field, it reaches to its zero value. Increasing the magnetic field, it is started either from the lower nucleation field or from the zero magnetic-field value, where the superconducting state can exist for a large disk radius or a small angular momentum.

3.2 MEISSNER VS. GIANT-VORTEX STATE

As explained in previous section, a cylindrical symmetry for the vortex state is assumed, as its order parameter was written as $\psi(\vec{\rho}) = F(\rho)\exp(iL\varphi)$. Therefore, in this approach, the flux quantization in the superconductor in applied field is always realized through the formation of multi-quanta vortices, the so-called "giant" vortices. One should note that such vortices are found energetically unstable in bulk superconductors and plain films. However, in mesoscopic samples their appearance may be favored due to confinement effects. As we have seen in Sec. 1.2.2, in the Meissner state the superconductor repels the applied magnetic field by increasing the circulating superconducting current at the edges. Those screening currents may cause the compression of vortices present in the sample into a giant vortex. The formation of a giant vortex in mesoscopic disks has been recently confirmed experimentally [53].

Therefore, the one-dimensional approximation for the vortex state seems justified for small disks (with $R \sim \xi$) where boundaries play an important role. We find the stable solutions of the Ginzburg-Landau (GL) equations as follows. First, for given vorticity L, from the linearized GL equation [Eq. (3.11)] we find $F(\rho)$ up to a multiplying constant. This function is then inserted into the free energy expression (3.9) which after minimization determines: (i) the constant in $F(\rho)$, and (ii) the energy value corresponding to the found state.

3.2.1 Reentrant behavior in the ground state

The dependence of the free energy on the magnetization of the magnetic coating M is shown in Fig. 3.2 for different sizes of the superconducting (SC) disk. The magnetic coating (ring) was taken of width $R_{out} - R_{in} = 1\xi$ (see Fig. 3.1). Note however that inner radius of the magnetic coating was changed correspondingly to the size of the superconducting sample. Consequently, the profile of the applied magnetic field for different SC disks was different (see Sec. 2.2).

Even on first sight, one notices large differences in the present diagram in comparison to the case of homogeneous magnetic field
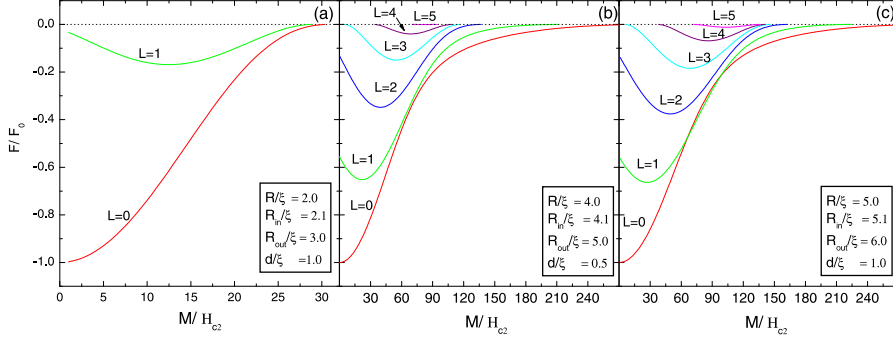
Fig. *3.2*   Gibbs free energy as a function of the applied magnetic field, for supercon-
ducting disks with radius $R = 2\xi$ (a), 4ξ (b) and 5ξ (c), with magnetic coating of width
1ξ. The thickness of the structure is taken $d = 1\xi, 0.5\xi$, and 1ξ respectively. The su-
perconductor and ferromagnet are seperated by an oxide layer, typically of thickness
$l = 0.1\xi$.

discussed in section 1.2.2 (Figs. 1.11). For radius of the SC disk
of $R = 2\xi$ [Fig. 3.2(a)], only the Meissner state and the single
vortex state ($L = 1$) were found stable, as the disk appears to
be too small to capture more vortices. However, even the $L = 1$
state appears only as *metastable* state, i.e. stable, but with higher
energy than the ground-state. The lowest-energy equilibrium at
all magnetic fields was reserved for the vortex-free Meissner state.
Same behavior of the SC state was found for larger disk with
$R = 4\xi$ [Fig. 3.2(b)], with the exception that states with larger
vorticity were also found to be stable. However, *no transition* (i.e.
crossing) was found between any two stable vortex states. Instead,
vortex states occupy separate energy levels, with higher-vorticity
states having higher energy. The reason for such differentiation
of the vortex states lies in the highly inhomogeneous magnetic
field profile in the sample. Namely, thin magnetic ring emits stray
magnetic field with sharp peaks close to its inner edges, which
decay fast towards the center of the structure. As giant vortex
states are imposed by the cylindrical symmetry of the sample,
their energetically favorable position is in the center, where low
magnetic field is unable to support their nucleation. At the same
time, the profile of the applied magnetic field is ideal for expulsion
from the sample, with its maxima being located close to the edges.

This feature obviously favors Meissner state as the lowest-energy one.

However, this picture changes for larger disk with $R = 5.0\xi$, whose energy is given in Fig. 3.2(c), where we observed the $L = 0 \rightarrow 1 \rightarrow 0$ crossing in the ground-state. Due to increased size of the disk, the magnetic field profile becomes more evenly distributed in the central part of the disk. While maxima of the field still strongly suppress superconductivity close to the disk edges, it becomes more favorable for the superconductor to nucleate a single vortex in its center, than to suffer the depletion of the order parameter by the Meissner currents in whole its area. Nevertheless, these competing effects favor once more the Meissner state at higher magnetization of the coating, resulting in the $L = 0 \rightarrow 1 \rightarrow 0$ reentrant behavior of the ground-state. Such reentrance of the vortex state with *lower* vorticity when magnetic field is *increased* is clearly counterintuitive and to our knowledge unique. In a purely theoretical concept, similar behavior was actually predicted in Ref. [5] for disks with a localized inhomogeneous magnetic field with zero average in the center. Therefore, the only known and experimentally observable reentrant behavior of the ground-state is the configurational one (multi-vortex→ giant→multi-vortex) found for disks with enhanced surface superconductivity [43].

To better understand the nature of the $L = 0 \rightarrow 1 \rightarrow 0$ crossing, we took a closer look on the current and order-parameter distribution in the sample for different values of the coating-magnetization. Fig. 3.3 shows the Cooper-pair density and current distribution for a disk in the Meissner state and $R = 2\xi$ (a, b) and $R = 5\xi$ (c, d), thus corresponding to Figs. 3.2(a, c). As explained before, SC disk with radius 2ξ always manages to screen the stray magnetic field of the coating, regardless of the magnetization of the material. Since the stray field is maximal at the disk edges, the profile of the induced supercurrent is different from the one in the case of a homogeneous magnetic field (see Fig. 3.3(c) vs. Fig. 1.12(b)). Figs. 1.12(b, e) also show that with increasing homogeneous field the Meissner current at the edge monotonously increases before the vortex entry in the ground state. In the present case the tendency is the same up to magnetization $M = 150H_{c2}$ when current
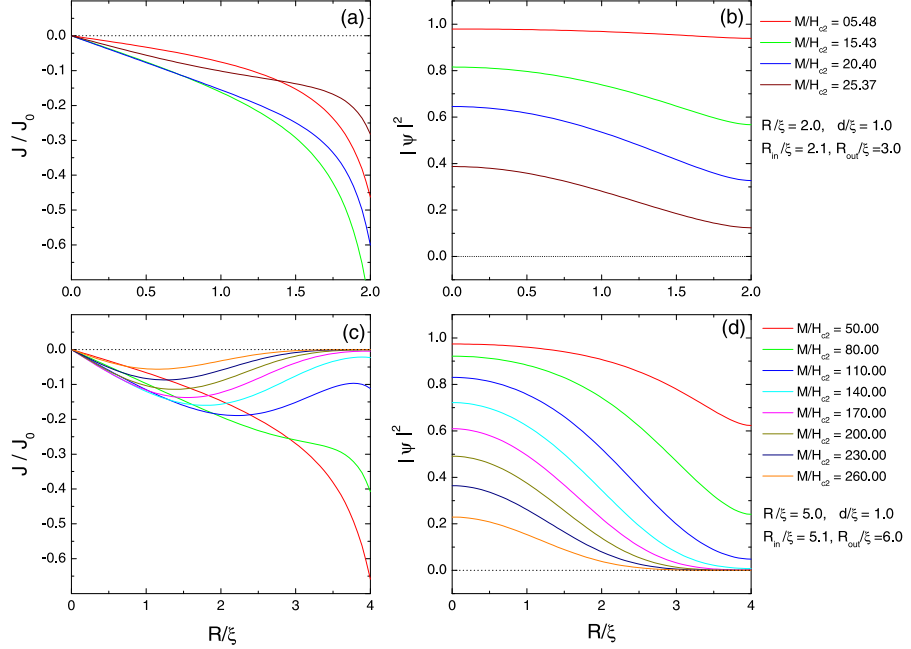
Fig. 3.3 The current density (a, c) and the Cooper-pair density (b, d) profiles for the samples in the $L = 0$ state, corresponding to Fig. 3.2 (a) and (c), respectively, for different magnetization of the magnetic coating.

starts *decreasing* due to the overall suppression of the Cooper-pair density. This is particularly pronounced for the larger sample and is actually the reason for the reentrant behavior. Namely, for $R = 5\xi$, after magnetization $M = 80H_{c2}$ is reached, not only the edge screening currents decrease, but they also *change their qualitative behavior*. The current on the edge drops to zero, and the maximum shifts to the inner part of the sample [see Fig. 3.3(c)]. At the same time, the Cooper-pair density becomes completely suppressed at the disk edge, where applied magnetic field is maximal [Fig. 3.3(d)]. Such a superconducting state, with ring-like singularity of the order-parameter, gains lower energy than the $L = 1$ vortex state, and becomes the ground-state at $M = 120H_{c2}$, as shown in Fig. 3.2(c). Still, it remains unclear if this "ring" state presents a separate phase emerging from the Meissner state through a second order transition, or it is an allotropic modification of a $L = 0$ state.

3.2.2 Stability of the "ring vortex"

The so-called "ring vortex" has been predicted in 1999 by Akkermans *et al.* [27], as a trivial solution of the linear Ginzburg-Landau theory for cylindrically symmetric superconductors. Since close to the superconducting/normal phase transition the non-linear term in Eq. (3.8) becomes negligible, it is intuitive that the superconducting state might nucleate in any form obeying the linearized GL equation.

In this section, we check the stability of a true "ring vortex" in our system, compared to the already observed state similar to it by appearance. For this purpose, we first solve numerically Eq. (3.11), and find the eigenvalues Λ and eigenfunctions f of the operator $\hat{L}$ from

$$\hat{L}f_{n,L}(\rho) = \Lambda_{n,L}f_{n,L}(\rho), \tag{3.12}$$

where $f_{n,L}(\rho)$ satisfies the condition $\rho(\partial f/\partial \rho)|_{\rho=0} = 0$ at the disk center. The index n=1,2... enumerates the different excited states for the same L-value, ordered by energy (with $n = 0$ denoting the lowest-energy solution).

In numerics, the finite difference technique were employed where the order parameter was put on a space grid and found numerically the eigenvalues of the operator $\hat{L}$ using the Householder technique. The resulting eigenfunctions for different sizes of the sample are shown in Fig. 3.4. Here the newly introduced index n shows its true nature, as it denotes the number of zeros in the order parameter in the radial direction.

These eigenfunctions of the linear GL operator are then incorporated in the full, non-linear formalism, where they are presumed to be the final solution up to a multiplying constant. However, the iteration procedure described in Sec. 3.1 always delivered the same outcome - the $L = 0$ state, already shown in the preceding section. The energy of the "ring vortex" as a solution of the linear theory and the energy of the final $L = 0$ state are shown in Fig. 3.5 for different sizes of the sample.

To conclude, we were not able to realize the "ring vortex" as a separate phase from the usual $L = 0$ case. Similarly to Ref. [5] where superconducting disk with magnet on top was studied, the ring-like solutions of the linear theory did not minimize the full
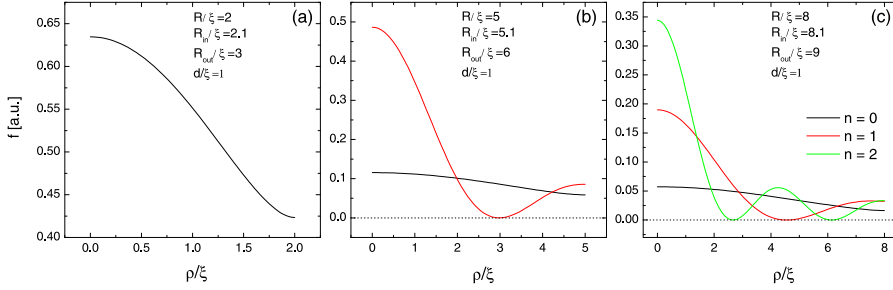
Fig. *3.4*   The eigenfunctions of the linear Ginzburg-Landau operator for the ground state [$n = 0$, (a)], and excited states [$n = 1, 2$, (b,c)] for samples with zero angular momentum (L=0).
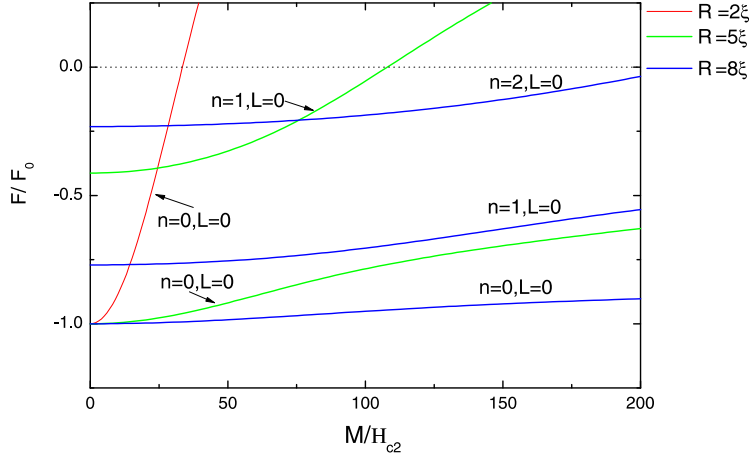

Fig. *3.5*   The free energy for excited states ($n > 0$) and the lowest-energy state, obtained from linear Ginzburg-Landau theory for angular momentum zero, shown for three superconducting disks with parameters of Fig. 3.4.

Ginzburg-Landau functional. We should clarify here that "ring vortex" is no vortex at all, since it is not possible to close a contour around it with a phase change of 2π. Even the realized cylindrically symmetric full suppression of the order parameter seems to be less physical and more an artifact of the used one-dimensional model. Therefore, further investigation with more degrees of freedom is warranted.

4

Two-dimensional approach

It is already generally accepted that for very thin superconductors ($d < \lambda, \xi$) in perpendicular magnetic field, the order parameter, current and the vector potential do not vary significantly over the sample thickness. In other words, their z-dependence may be ignored, and the boundary condition of Eq. (3.8) is automatically fulfilled at top and bottom surfaces of the sample (for details see Sec. 3.1). In this way, the fully three-dimensional problem can be reduced to a two-dimensional one. We use this property of thin superconductors and average the Ginzburg-Landau equations over the sample thickness. Thus in this chapter we will address the topic of the preceding chapter by using the two-dimensional approach, where no cylindrical symmetry of the system (i.e., the superconducting state) is presumed.

Formally, theoretical model remains the same. In the extreme type-II limit, the Ginzburg-Landau functional from Eq. (3.5) reads

$$ F = \frac{G_{sH} - G_{nH}}{H_c^2(V/8\pi)} = \int \{-2|\Psi|^2 + |\Psi|^4 + 2|(-i\vec{\nabla} - \vec{A_0})\Psi|^2\} dV, \ (4.1) $$

where G_{nH} is the free energy of the normal phase when an external field (inhomogeneous in general) $\vec{H_0} = rot\vec{A_0}$ is applied.

Using several mathematical transformations, the superconductor-vacuum boundary condition [Eq. (3.3)] and the first GL equation [Eq. (3.1)], the free energy expression in extreme type-II case and/or in the case of extremely thin superconductors becomes

$$F = -\frac{H_c^2}{4\pi} \int |\Psi|^4 d\vec{r}. \tag{4.2}$$

For completeness, we repeat once more the dimensionless first Ginzburg-Landau equation

$$(-i\vec{\nabla} - \vec{A}_0)^2\Psi = \Psi(1 - |\Psi|^2), \tag{4.3}$$

and the equation for supercurrent density

$$-\vec{j}_{2D} = \frac{1}{2i}(\Psi^*\vec{\nabla}_{2D}\Psi - \Psi\vec{\nabla}_{2D}\Psi^*) - |\Psi|^2\vec{A}_0. \tag{4.4}$$

The boundary condition on the SC-vacuum interface remains

$$\vec{n} \cdot (-i\vec{\nabla}_{2D} - \vec{A})|_{boundary} = 0, \tag{4.5}$$

that is, no supercurrent can pass perpendicularly through the disk surface.

Indices 2D only emphasize that these two equations will be solved numerically in Cartesian coordinates, allowing the solutions to break the cylindrical symmetry.

Numerical scheme: Now, our discretization technique will be explained. To find the stationary solution of the equation (4.3), according to Kato *et al.* [44] we can start from its time-dependent form

$$\frac{\partial\Psi}{\partial t} = -\frac{1}{12}\left[\left(\frac{\vec{\nabla}}{i} - \vec{A}\right)^2\Psi + (1 - T)\left(|\Psi|^2 - 1\right)\Psi\right] + \tilde{f}(\vec{r}, t), \tag{4.6}$$

where T is temperature and $\tilde{f}(\vec{r}, t)$ is a dimensionless random force. Next essential step is the introduction of the link variable between $\vec{r}_1$ and $\vec{r}_2$ as

$$U_\mu^{\vec{r}_1, \vec{r}_2} = \exp\left[-i\int_{\vec{r}_1}^{\vec{r}_2} \vec{A}_\mu(\vec{r}) \cdot d\vec{\mu}\right], \tag{4.7}$$
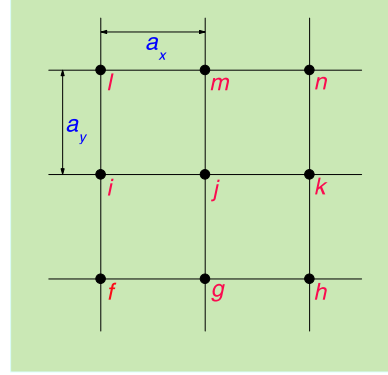
Fig. 4.1 Schematic diagram of the uniform Cartesian grid-point lattice used in the simulations (from Ref. [44])

with $\mu = x, y$, which puts the gauge field A on the links of the computational lattice. In the calculation, the whole system is mapped on a uniform square Cartesian grid (see Fig.4.1).

Let us now demonstrate how different terms in Eq. (4.6) are rewritten using the link variable. As example, the first term on its right side is taken, in the grid point j and can be written as

$$\left(\frac{\nabla_\mu}{i} - A_\mu\right)^2 \Psi_j = -\nabla_\mu^2 \Psi_j + i\nabla_\mu(A_\mu \Psi_j) + A_\mu^2 \Psi_j + iA_\mu \nabla_\mu \Psi_j$$

$$= \frac{1}{U_\mu^j}\left(-2iA_\mu U_\mu^j \nabla_\mu \Psi_j - iU_\mu^j \Psi_j (\nabla_\mu A_\mu - iA_\mu^2) + U_\mu^j \nabla_\mu^2 \Psi_j\right) (4.8)$$

After substituting $\nabla_\mu U_\mu^j = -iA_\mu U_\mu^j$ and $\nabla_\mu^2 U_\mu^j = -iU_\mu^j(\nabla_\mu A_\mu - iA_\mu^2)$, and some trivial transformations, we obtain for $\mu = x$ (analogously for $\mu = y$)

$$\left(\frac{\nabla_x}{i} - A_x\right)^2 \Psi_j = \frac{1}{U_x^j}\frac{1}{a_x}\left(\frac{U_x^k \Psi_k - U_x^j \Psi_j}{a_x} - \frac{U_x^j \Psi_j - U_x^i \Psi_i}{a_x}\right)$$

$$= \frac{U_x^{kj}\Psi_k - 2\Psi_j + U_x^{ij}\Psi_i}{a_x^2}, \qquad (4.9)$$

where indices i, j, k denote the corresponding grid points, illustrated in Fig. 4.1.

Finally the discretized time-dependent Ginzburg-Landau equation can be written as

$$
\begin{aligned}
\frac{\Delta \Psi}{\Delta t} \;=\; & \frac{1}{12}\left[\frac{U_x^{kj}\Psi_k}{a_x^2} + \frac{U_x^{ij}\Psi_i}{a_x^2} + \frac{U_y^{mj}\Psi_m}{a_y^2} + \frac{U_y^{gj}\Psi_g}{a_y^2}\right. \\
& \left. -\frac{2\Psi_j}{a_x^2} - \frac{2\Psi_j}{a_y^2} + (1-T)\left(|\Psi_j|^2 - 1\right)\Psi_j\right] + \tilde{f}_j(t) \quad (4.10)
\end{aligned}
$$

Since in our simulations an uniform grid is used, in the upper expression a_x equals a_y.

Eq. (4.10) is use when in solving Eq. (4.3) for the applied vector potential (from the magnetic coating, A_0 as denoted earlier). First, the linearized GL equation is solved, by setting the non-linear part to zero. This solution is then substituted in the non-linear equation, a new solution is found, and substituted back in the equation. For time-relaxation, the number of iterations and the chosen time-step [Δt in Eq. (4.10)] are essential and depend on the complexity of the vortex structure. The random force $f(t)$, uncorrelated in space and time ensures that only true equilibrium is found as a stable solution. In this recurrent procedure based on a Gauss-Seidel technique, convergence is finally reached and the first GL equation is solved [14] for the order parameter Ψ in every grid point. These values now used in equation (4.4) to calculate the current densities j_x and j_y as

$$
j_{x,y} = \frac{1}{2}\left[\Psi^*\left(\frac{1}{i}\frac{\partial}{\partial x, y} - A_{x,y}\right)\Psi + \Psi\left(\frac{1}{i}\frac{\partial}{\partial x, y} - A_{x,y}\right)^* \Psi^*\right] \quad (4.11)
$$

where again link variable approach comes into play through similar transformations as in Eqs. (4.8-4.9)

$$
\left(\frac{1}{i}\nabla_x - A_x\right)\Psi_j \rightarrow -i\frac{1}{U_x^j}\nabla_x(U_x^j\Psi_j) = -i\frac{U_x^{kj}\Psi_k - \Psi_j}{a_x}, \quad (4.12)
$$

and

$$
\left(\frac{1}{i}\nabla_y - A_y\right)\Psi_j \rightarrow -i\frac{1}{U_y^j}\nabla_y(U_y^j\Psi_j) = -i\frac{U_y^{mj}\Psi_m - \Psi_j}{a_y}. \quad (4.13)
$$

In this way the first GL equation is solved for fixed applied magnetic field. Once a solution is obtained at a given magnetic field,

the field is increased (or decreased) and this solution is used as the initial value in the new calculation. In doing so, the program stays within the same local minimum of the free energy and follows this minimum as a function of the magnetic field as long as it is stable. The calculations were also repeated with $|\Psi|^2 \approx 1$ and $|\Psi|^2 \approx 0$ is taken in the whole sample, as initial condition. In all these runs, we summarize the found solutions and construct a complete energy spectrum of stable vortex states as a function of applied magnetic field.

4.1 MEISSNER VS. MULTIVORTEX STATES

In Fig. 4.2, we present the free energy as obtained from the present 2D approach (b) and compared to the energy calculated for the same parameters using the 1D approach from the previous chapter (a). The results for the superconducting disk of radius 4ξ with magnetic coating 2ξ wide, show striking discrepancy between the two approaches.

First of all, the reentrant behavior of the Meissner phase in the ground-state *seems not to appear* in the free energy diagram where cylindrical symmetry is not taken a priori [Fig. 4.2(b)]. Moreover, the Meissner state is stable only up to magnetization $M = 52H_{c2}$, after which a vortex enters the sample. The contour-plot of the Cooper-pair density and the superconducting phase of the $L = 1$ state are shown in Fig. 4.3(a, b). Further increase of the magnetization (i.e., the stray field of the magnet) favors entry of additional vortices, similarly to the case of superconducting disks in homogeneous magnetic field [14]. However, as the main result of the two-dimensional model, the vortex states of higher angular momenta *are not giant vortices*, but sets of individual flux lines arranged on a ring (see Fig. 4.3(a-h)). Each vortex has an individual path of 2π phase change around itself, and contributes to the $L \times 2\pi$ phase change on the periphery of the disk (see Fig. 4.3 and Sec. 1.2.1). In superconducting terminology, such states are called *multivortex states*, and are described by a set of singularities in the superconducting order parameter surrounded by circulating supercurrents (see Fig. 4.4), each carrying a flux quantum. Therefore, in a sense, multivortex state is an analogue of the

Abrikosov vortex lattice in bulk, but now strongly influenced by the topological confinement.

Therefore, the main difference between the 1D and 2D models is in the nucleation of multivortex states for given vorticity L. Namely, it is energetically more favorable for individual vortices to sit in the region away from the center of the disk, where the applied magnetic field is maximal. This was not allowed in the 1D approach. For the considered size of the superconducting disk, the maximal vorticity found is $L = 4$, before superconductivity is destroyed. However, it is noticed that beyoned M/H_{c2}=104.01, $L = 4$ line in Fig. 4.2(b) stays stable up to very high magnetic fields. This is counterintuitive, as there is no reason for this state to be energetically favorable compared to states with other, higher or lower vorticities. For that reason, we studied the Cooper-pair density and phase plots for higher magnetizations of the coating, shown in Fig. 4.5. Interestingly enough, it appears that 4 vortices actually *leave the superconductor when magnetic field is increased*. Apparently, the repulsive interaction of vortices makes additional vortex entry impossible. Instead, vortices leave the sample, and are gradually replaced by a *complete destruction of superconductivity at the sample edge*. In this sense, since the resulting state is vortex-free, we may see it as a *newly appeared $L = 0$ state*, resembling a "ring vortex". Fig. 4.6 shows the radial position of vortices with increasing magnetic field when total vorticity in the system is 4 and they are evolving towards the edge.

Therefore, the reentrant behavior of the $L = 0$ state in the ground-state has been realized in the two-dimensional approach. As different from the 1D model, the conventional Meissner phase is now clearly separated from the $L = 0$ ring-like suppression of the order parameter at the disk edge [two separate lines in Fig. 4.2(b), vs. single $L = 0$ line in Fig. 4.2(a)]. To investigate this further, I enlarge the superconducting disk in pursue of more complex vortex configurations.

4.2   STABILIZATION OF INDIVIDUAL VORTICES CLOSE TO THE SC-FM INTERFACE

As discussed in section 2.2.3, the magnetic field profile of a ferromagnetic ring (which is placed around the superconducting disk) varies strongly with changes in the geometry. For example, larger inner radius and smaller width of the magnetic ring increase the amplitude of the magnetic field close to the inner edges of the magnet and decreases the stray magnetic field in the center of the ring. It is exactly such magnetic field profile that is aimed to impose on a somewhat larger superconducting disk than previously considered. In such a configuration, larger disk radius allows entry of more vortices in the sample, but they are likely to remain strongly confined close to the sample edge.

For a superconducting disk with $R = 7\xi$ surrounded by a magnet with $R_{in} = 7.1\xi, R_{out} = 8\xi$ and thickness $d = 1.0\xi$, Fig. 4.7 shows the contourplots of the $|\Psi|^2$-density, the corresponding phase change, and the vectorplot of the supercurrents, for the states with five (a) and eight (b) vortices. The applied inhomogeneous field profile, created by the ferromagnetic ring, across the superconducting disk, is shown in Fig. 4.7(c). Larger superconducting disk however favors the expulsion of the magnetic field, especially if the field is inhomogeneous and maximal at the disk-edges (such as the stray field of the magnet in our case). Consequently, rather large magnetization of the magnetic material is needed to achieve vortex nucleation in these samples, e.g. $M \approx 390H_{c2}$ and $M \approx 525H_{c2}$ are sufficient for 5 and 8 vortices, respectively (shown in Fig. 4.7). All nucleated vortices however are located within 20% from the sample edge, and they maximize their inter-distance as vorticity increases. For that reason, certain saturation vorticity can be defined, after which the ring-line normal core at the disk edge becomes lower in energy than a set of individual vortices in a shell (similar to the ones shown in Fig. 4.5). From a fundamental point of view, we should also emphasize that single vortex shell at large vorticities is not energetically favorable in SC disks in a homogeneous magnetic field. The latter case behaves similarly to the confined systems of charged particles [38], where multiple shells are formed for larger number of constituents.

Moreover, it has been theoretically predicted for classical clusters, and experimentally confirmed in the case of vortices in SC disks [58], that maximal number of particles in the first shell can not exceed five. As we just showed, in our SC disk with magnetic coating around, depending on disk size, *arbitrary number of vortices* can be stabilized in a single vortex shell.

4.3   NOVEL PHASE TRANSITIONS

Of course, this last statement is only partially correct. Namely, stabilization of a large number of vortices requires large magnetic field, i.e., large magnetization of the coating. If so, one can expect that initially low value of the magnetic field in the center of the sample may also become significant when multiplied by M. To grasp the complete picture, we will now investigate all stable vortex states in the disk with radius $R = 8\xi$ surrounded by a magnet with $R_{in} = 8.1\xi, R_{out} = 9\xi$ and thickness $d = 2.0\xi$. The corresponding free energy as a function of magnetization of the magnetic ring is shown in Fig.4.8. The vorticity in the ground state changes gradually (by 1) as magnetization is increased. However, the maximal number of vortices in the disk, $L = 14$ is reached at $M = 681H_{c2}$ and no additional states are found above that threshold. Let us, however, first address the feature on the opposite side of the diagram - the nucleation of the very first vortex in the sample. Apparently, a very large Bean-Livingston barrier [37] for the vortex entry needs to be overcome, as the flux needed for the appearance of the first vortex is more than 5 times larger than the differentiate flux needed for the entry of additional vortices at higher magnetization. It is shown in Fig. 4.3 that $L = 1$ state in small disks with magnetic coating has a single vortex in the center of it, due to the very strong lateral confinement. However, one should immediately notice that such a location is not really favorable for the vortex, taking into account that applied magnetic field is low there. In other words, the question of the location of the vortex in the $L = 1$ state is not a trivial one and is a result of two competing effects, the boundary pushing the vortex towards the disk center, and the (non-homogeneous) magnetic field energy pulling it closer to the disk edge. Therefore, and as shown in Fig.

4.9(a), the equilibrium position for a vortex may be *displaced from the center of the structure*. As a result, the $L = 1$ state exhibits very untypical *asymmetry* with respect to the sample geometry. The reason for this effect is (i) the necessity for flux quantization in superconductors, and only then (ii) minimization of the energy of the vortex with respect to the applied magnetic field profile. For example, similar inhomogeneous magnetic field profile would never be enough to solely break the symmetry of the electron probability density in cylindrical semiconducting quantum dots.

When magnetization is increased, more vortices enter the sample, and are arranged on a ring close to the sample edge, as discussed previously. This tendency is preserved up to vorticity 12, when one vortex *percolates the enterior of the disk*, with remaining 11 still located on the edge [see Fig. 4.9(b)]. Interestingly enough, further added vortices at higher magnetization are not able to penetrate inside the disk, being repelled by the first one, and squeeze in the outer vortex shell, up to the maximal vorticity $L = 14$. Similarly to the case described for the reentrant behavior of the $L = 0$ state in small samples (Sec. 4.1), with increasing magnetization the vortex shell leaves the superconducting disk through a second order transition, in which it is replaced by a ring-like, completely normal core. At the same time, the central vortex is not influenced by this process and remains in the sample. Being so, we are de facto realizing the *reentrance of $L = 1$ state* in the ground state. One can expect that for properly chosen parameters (i.e. disk and magnet sizes) more vortices can enter the central disk region, in which case one could observe the re-appearance of any small L-state.

We should also comment here on the inability of the superconducting disk to nucleate more vortices after superconductivity has been destroyed at its edges (e.g. for $M > 717H_{c2}$). To understand this, we must consider two types of boundary conditions, so-called Neumann and Dirichlet ones. Namely, as we mentioned on several occasions, we use boundary conditions for the current perpendicular to the disk surface being zero (i.e. Neumann condition). However, after superconductivity has been completely suppressed at the sample edges, our boundary gradually transforms into a

Dirichlet type, i.e. simply vanishing of the superconducting order parameter - $\Psi = 0$.

The influence of these boundary conditions on the vortex entry in mesoscopic superconducting cylinders has been previously considered in Ref. [48]. It has been found that the main characteristics of the superconducting-normal boundary, since the superconducting order parameter vanishes at the surface, is that the Meissner shielding currents are nucleated at a distance of a few ξ inside the sample, instead of being right at the boundary. Therefore, the number of vortices that can stay inside the sample decreases for a given magnetic field, when compared with the superconducting-insulator boundary. In Fig. 4.9(c) we show that while superconductivity is destroyed at the boundary of our sample, maximal Meissner currents flow at a certain distance inside the the disk. We conclude that our superconducting disk becomes effectively smaller, and the situation fully agrees with the above discussion of the superconducting-normal interface. Note also that the presence of a normal layer at the disk edges has additional fundamental consequences, as it obviously disables the mechanism of *surface superconductivity*, during the onset of the superconducting state from the normal state in decreasing magnetic field.
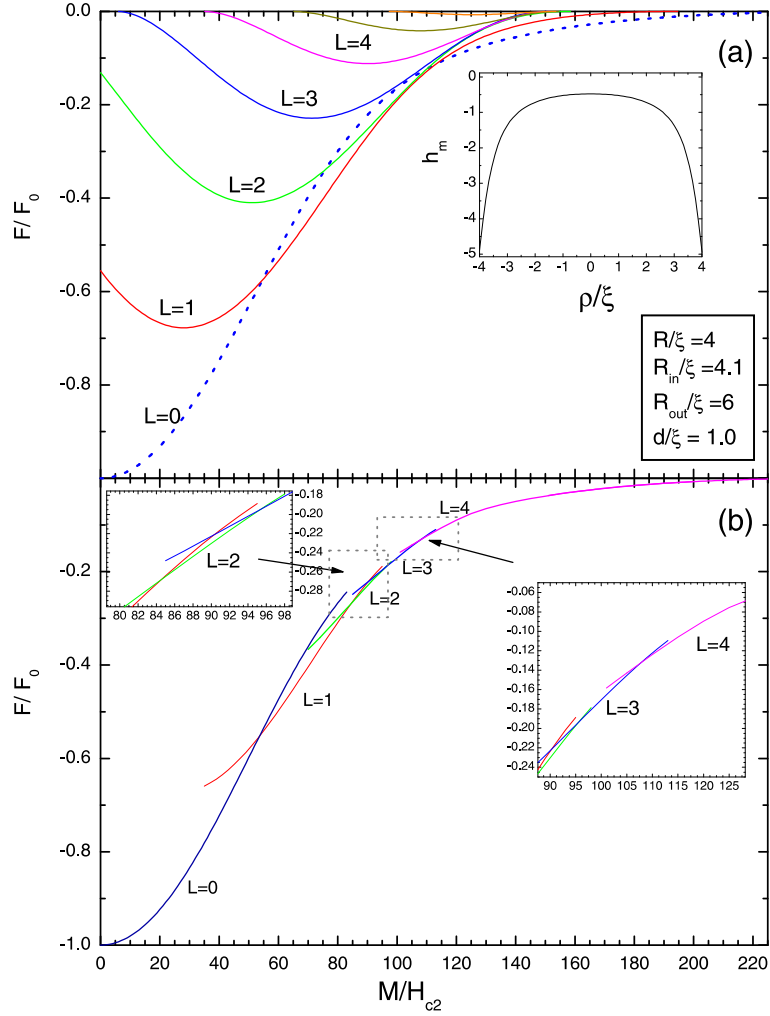
Fig. 4.2   (a) The free energy of the giant vortex states with different angular momenta
L as a function of the magnetization of the magnetic coating, for $R = 4\xi$, $R_{in} = 4.1\xi$,
($l = R_{in} - R = 0.1\xi$) and $R_{out} = 6\xi$ with thickness $d = 1.0\xi$ (obtained from the one-
dimensional model). Inset shows the stray magnetic field profile inside the magnetic
ring. (b) shows the free energy calculated in the two-dimensional approach, for the
same parameters and angular momenta as in (a). Two regions are zoomed out as
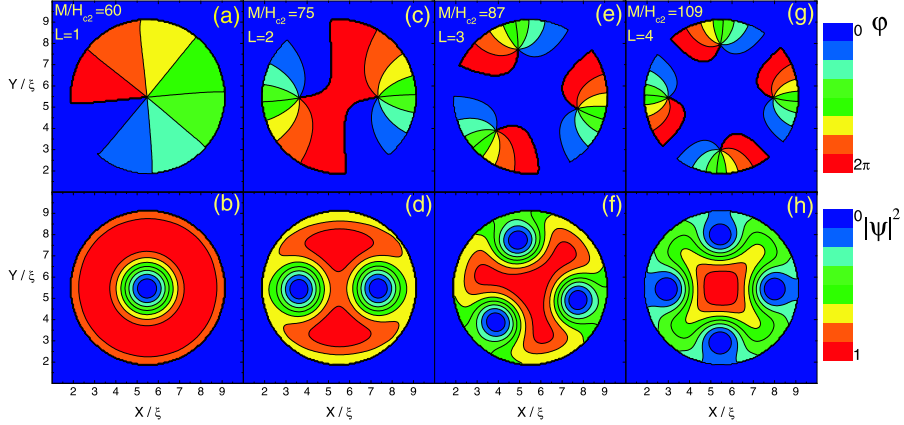insets for clarity.

Fig. 4.3 Contourplots of the $|\Psi|^2$-density for the ground state and the corresponding phase for different values of the magnetic field and different vorticity ($R = 4\xi$, $R_{in} = 4.1\xi$, and $R_{out} = 6\xi$, with thickness $d = 1.0\xi$, see Fig. 4.2).
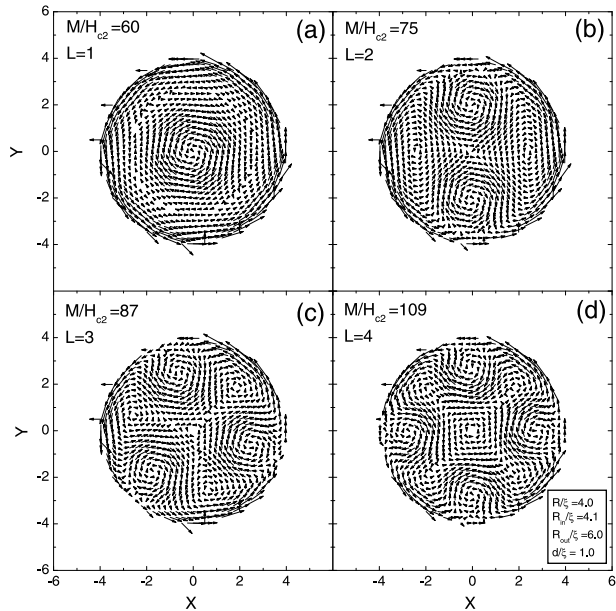

Fig. 4.4 Vectorplots of the supercurrents corresponding to the states shown in Fig.-4.3.
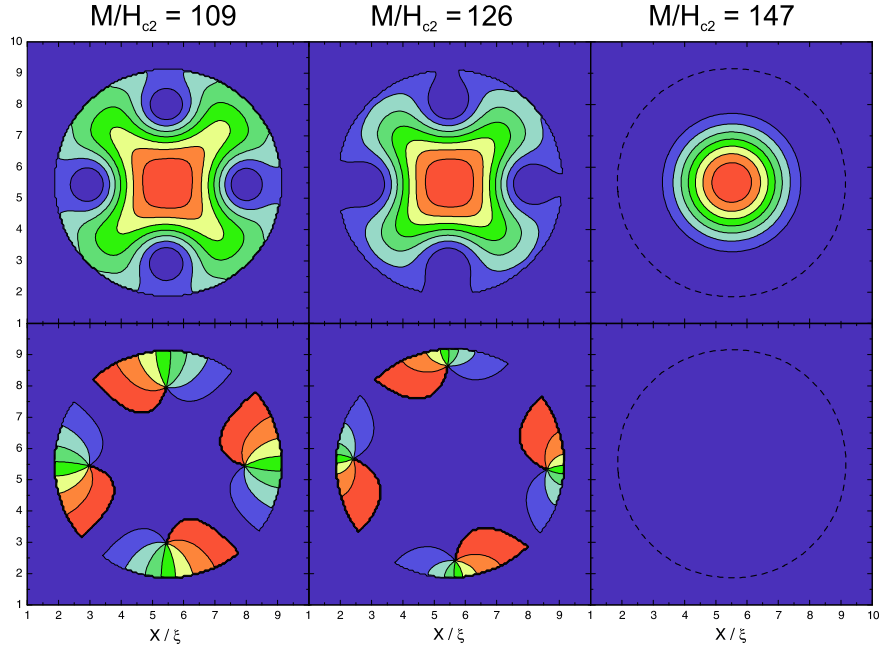
Fig. 4.5 The Cooper-pair density contour plots and corresponding phase during the second-order vortex exit from a disk with $R = 4\xi$, with magnetic coating of high magnetization (see Fig. 4.2(b), magenta curve).
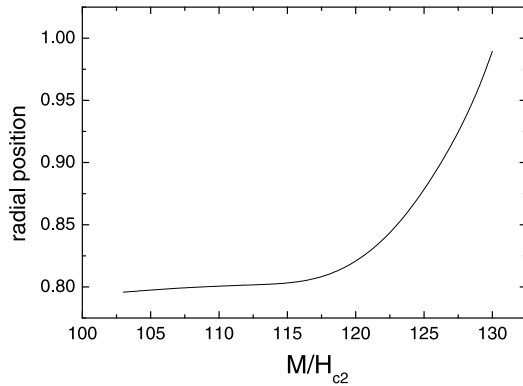

Fig. 4.6 Radial position of vortices as a function of the magnetization of the magnetic coating corresponding to $L = 4$ vortex state (magenta curve in Fig. 4.2(b)). The position is measured in unit of the radius of the disk.
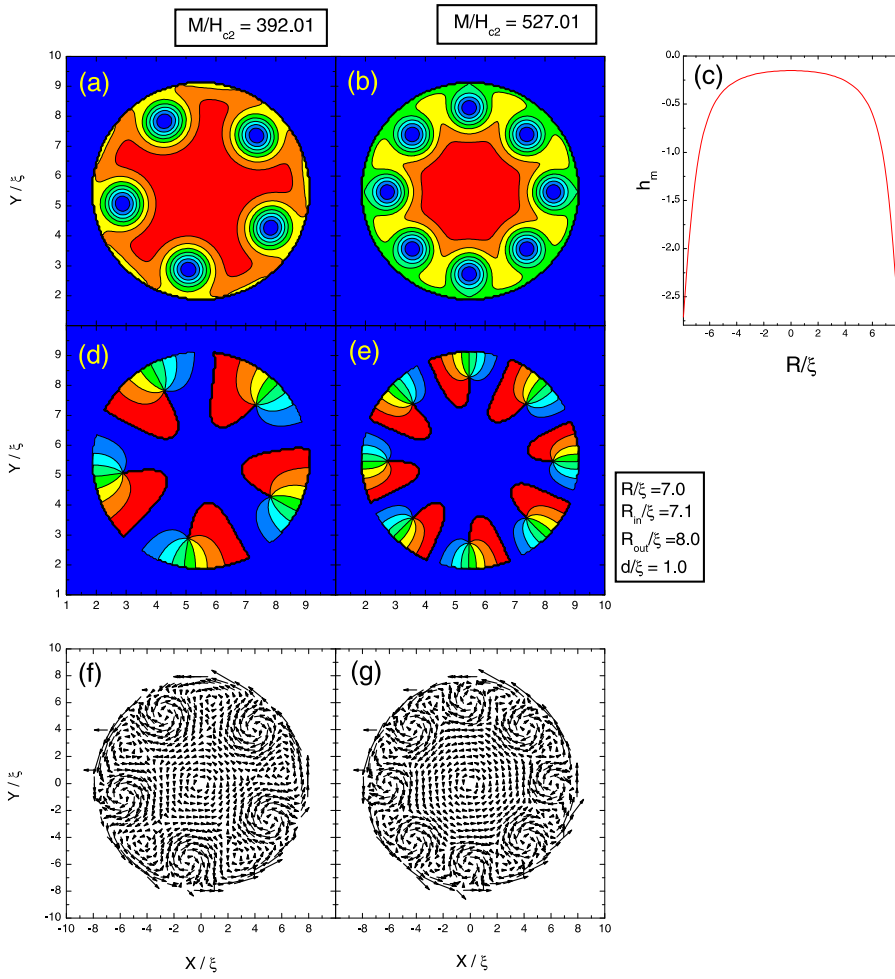
Fig. 4.7 Contourplots of the Cooper-pair density (a, b) for the ground state, the corresponding phase contourplots (d, e), and vectorplots of the current (f, g), for different values of the magnetization of the magnetic ring. Here $R = 7\xi$, $R_{in} = 7.1\xi$ and $R_{out} = 8\xi$ with thickness $d = 1.0\xi$. (c) shows the magnetic profile of the stray field across the superconductor.
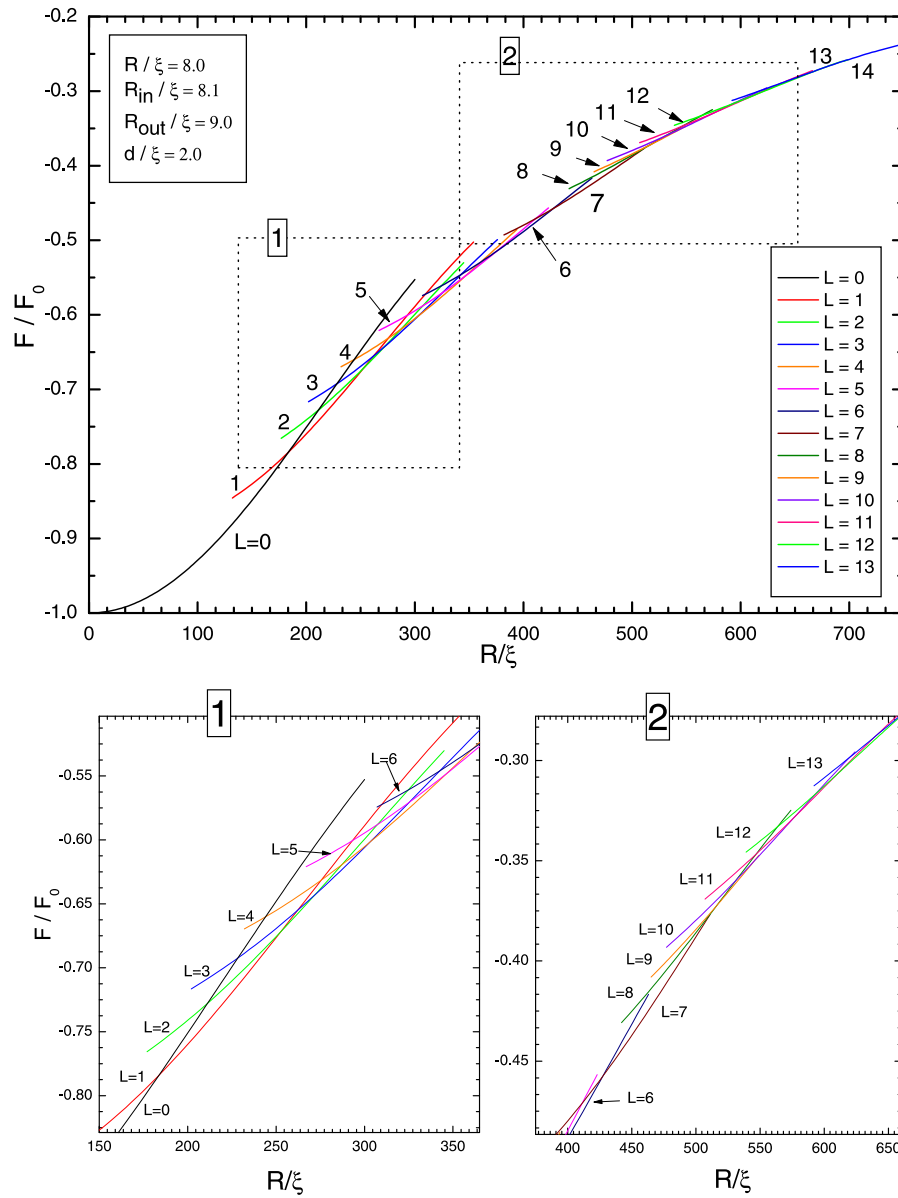
Fig. 4.8 The Gibbs free energy of the superconducting disk of size $R = 8.0\xi$, as a function of the magnetization of the magnetic coating with $R_{in} = 8.1\xi$, $R_{out} = 9.0\xi$ and thickness $d = 2.0\xi$. Areas 1 and 2 are zoomed out for clarity.
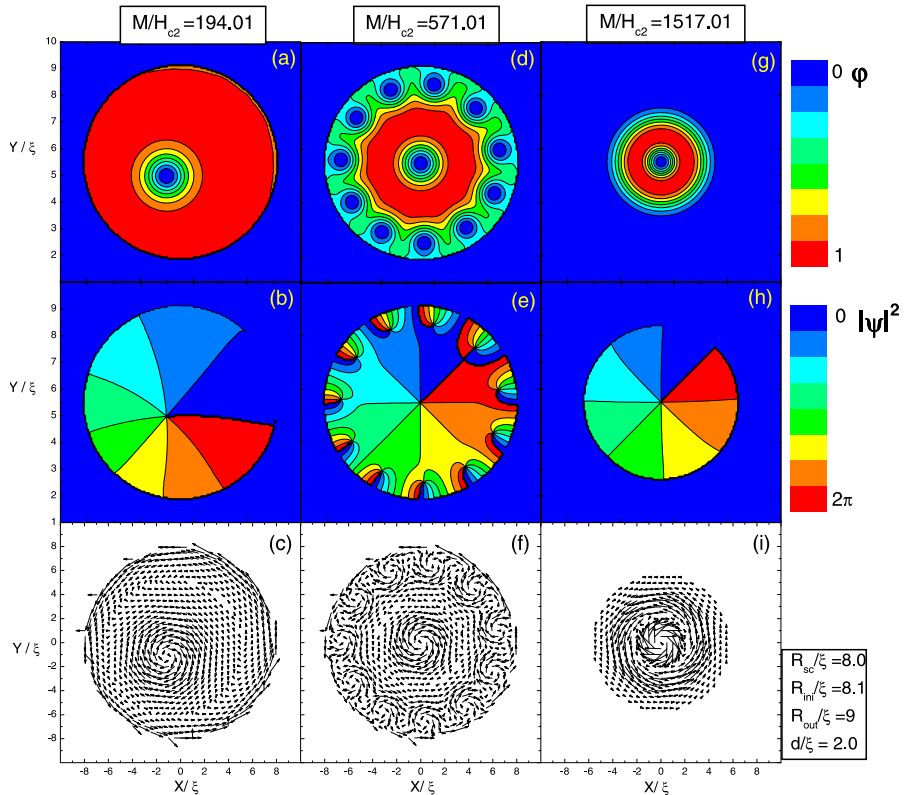
Fig. 4.9 Contour plots of the superconducting density (a,d,g) for the ground state and the corresponding phase contour plots (second row) for different values of the magnetic field. Here $R = 8\xi$, $R_{in} = 8.1\xi$ and $R_{out} = 9\xi$ with thickness $d = 2.0\xi$. Vectorplot of supercurrents also presented in 3rd row.

5

Co-axial SC-FM structure in a homogeneous magnetic field

In the present chapter we will explore the vortex structure of a superconducting (SC) disk with a ferromagnetic (FM) coating around, similarly to previous chapters, but now exposed to additional homogeneous external magnetic field (see Fig. 5.1). Superconducting structures, i.e. disks and films, with magnetic dots on top have been explored previously, and have shown several novel physical effects in additional homogeneous magnetic field. First, weakly magnetized magnetic dots with out-of-plane magnetization were found to attract the external flux lines when their polarization was parallel to the direction of the applied field, and vice versa [59]. This behavior is essential for the so-called *vortex pinning*, which in turn increases critical current of the structure, very relevant for potential applications. Second, previous works already established and explained the field-induced superconductivity phenomenon in the SC-FM structures [51, 60]. Namely, as one can easily imagine, superconductivity can be strongly suppressed by the neighboring magnetic dots, in which case, additional homogeneous magnetic field would compensate part of the inhomogeneous stray field of the magnets, and restore superconductivity in areas of the sample where compensation takes place. Third, in cases when magnetic dots create (anti)vortices themselves, their interaction with exter-
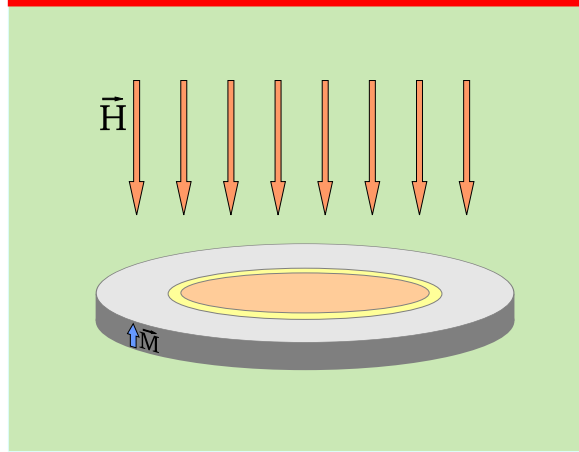
Fig. 5.1 Oblique view of the system: superconducting disk with magnetic coating in a homogeneous magnetic field (parameters indicated in the figure).

nal flux lines is quite complicated and may result in a number of novel and fascinating vortex configurations.

Motivated by all this, we consider basically same effects in our coaxial SC-FM sample. As we will show, chosen geometry of the structure brings new insight into the study of vortex configurations, pinning and enhancement of critical parameters of a superconductor.

5.1   CONTROLLABLE UPPER CRITICAL FIELD OF THE SAMPLE

In Figs. 5.2(a-c), we show the Gibbs free energy of the sample with the SC disk radius $R = 4.0\xi$ and thickness $d = 1.0\xi$, and magnetic coating with parameters $R_{in} = 4.1\xi$ and $R_{out} = 6\xi$, as a function of external homogeneous magnetic field. Fig. 5.2 gives complete free energy curves for each found vortex state in a sweep up and sweep down regime (increasing and decreasing magnetic field, respectively).

As shown in Fig. 5.2(a), in the case of demagnetized coating ($M = 0$), we reconstruct the case of a superconducting disk in a homogeneous magnetic field, similarly to what was discussed in Chapter 1.2 and Ref. [14]. The free-energy diagram is symmetric with respect to the polarity of the applied magnetic field, and
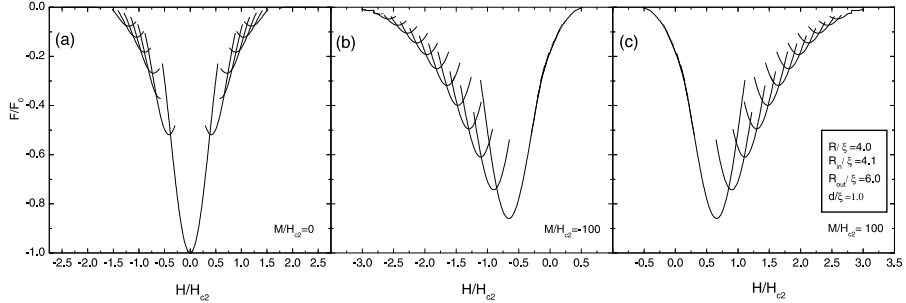
Fig. 5.2   The free energy of vortex states with different vorticity L as a function of the external magnetic field for $R = 4\xi$, $R_{in} = 4.1\xi$ and $R_{out} = 6\xi$, thickness $d = 1.0\xi$ (see Fig. 5.1), the magnetization of the FM coating (a) $M/H_{c2} = 0$, (b) $M/H_{c2} = 100$, and (c) $M/H_{c2} = -100$.

found vortex (or antivortex) states show same behavior for positive or negative external field. The ground state changes with increasing absolute value of applied field through states with increasing absolute vorticity, indicating the number of flux lines piercing through the SC disk. Note also that superconductivity ceases to exist at applied field of $H \approx \pm 1.52 H_{c2}$, thus upper and lower critical magnetic field are identical (in opposite polarity).

Let us now take fully magnetized FM coating with $M = -100 H_{c2}$, and repeat the calculation in applied homogeneous magnetic field. The stray magnetic field profile for such a coating has been shown previously as inset in Fig. 4.2(a). The results are shown in Fig. 5.2(b). The free energy curves show strikingly different behavior from the case of Fig. 5.2(a). As a main difference, the diagram is no longer symmetric with respect to the field-polarity. This asymmetry is threefold, and reflects to critical field, maximal vorticity, and behavior of vortex states with same absolute vorticity. The explanation of this phenomenon becomes obvious if one looks at the local magnetic field profile. Namely, for chosen directions of the magnetization of the FM coating and applied magnetic field (see Fig. 5.1), one notices that for negative magnetization M, the positive applied homogeneous field *adds* to it in the region where SC disk is located. In the same fashion, negative applied field *compensates* the stray field of the magnet inside the SC disk. For that reason, the upper critical field for our sample with $M = -100 H_{c2}$ is only $H = 0.53 H_{c2}$ while the
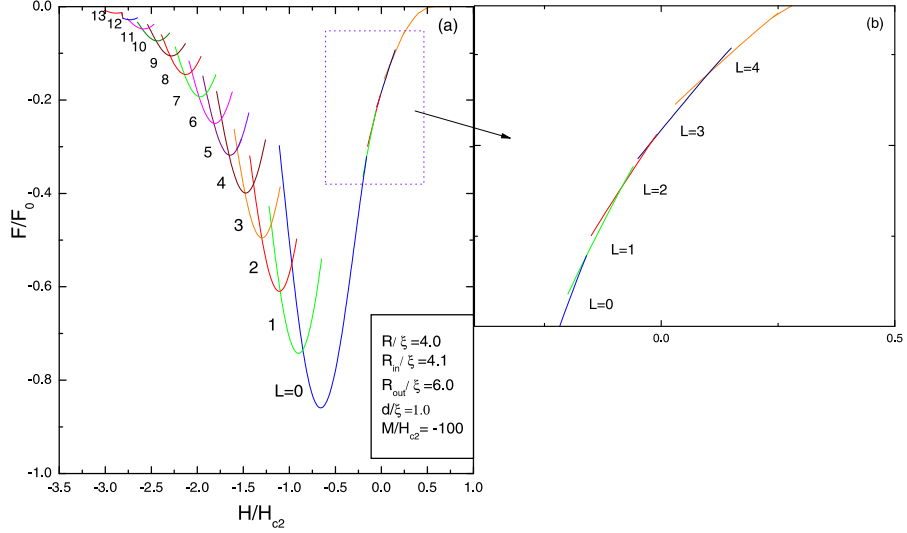
Fig. 5.3 (a) Gibbs free energy as a function of external magnetic field, for all found vortex states in negative and positive applied magnetic field H, and parameters corresponding to Fig. 5.2(b). (b) Area bounded by the dotted line in (a) has been enlarged here for clarity.

lower one is enhanced to $H = -3.11 H_{c2}$. Therefore, similarly to the case of field-induced-superconductivity [51], magnetic coating effectively enhances maximal applied magnetic field that superconducting disk can sustain, for given polarity of the field. This of course happens at expense of the critical field applied in opposite direction, where superconductivity is destroyed at lower field compared to the plain disk case. This situation is completely inverted if magnetization of the coating is reversed, as shown in Fig. 5.2(c). Therefore, the main message remains in the fact that upper critical field for given polarity of the applied field can be engineered in a very controllable fashion by proper choice of the parameters of the magnetic coating. This of course is of crucial importance for potential devices where superconducting elements may be of use.

5.2   FIELD-POLARITY DEPENDENT VORTEX STRUCTURE

The asymmetry in Fig. 5.2(b) is not pronounced only in the shape of the free-energy curves. The latter figure is now re-given in Fig.
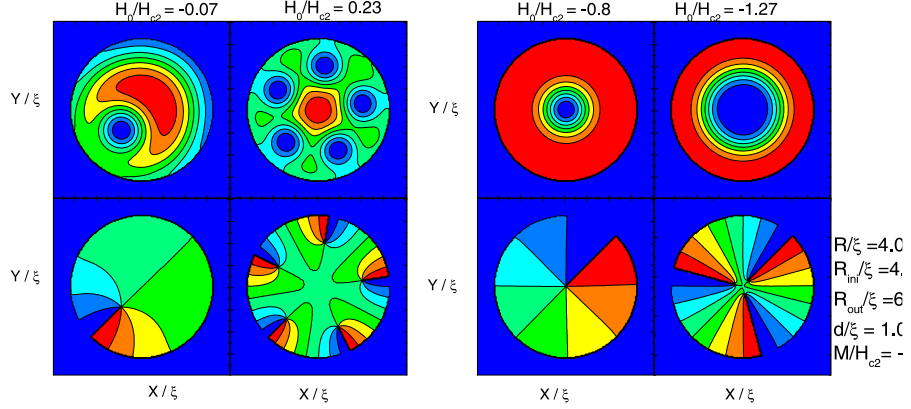
Fig. 5.4 Contourplots of the Cooper-pair density of the vortex states in the ground state, and the corresponding phase contourplots, for different values (see 5.3) of the applied magnetic field [left(right) panel - positive(negative) field].

5.3 with more details, and with some regions enlarged for clarity. First, it is obvious that maximal vorticity for $M = 0$ of $|L|_{max} = 7$ has been enlarged in negative applied field for $M = -100H_{c2}$ to $L^{-}_{max} = -13$, while maximal vorticity in positive fields has fallen to $L^{+}_{max} = 4$. Moreover, states with same absolute vorticity on opposite sides of the diagram, e.g. $L = -3$ and $L = 3$ significantly differ in their range of stability and behavior in applied field. At positive applied fields, the energy of states with positive vorticity always increases with increased field, whereas that is not the case at negative applied fields.

As we have explained earlier, the stray magnetic field of the coating is maximal along the edges of the superconducting disk, with amplitudes which may exceed by far the thermodynamic critical field H_c. Therefore it is easy to understand that if additional magnetic field is applied in the same direction as the stray field the superconductivity is easily destroyed. On that path, all additional vortices in the sample are located close to the disk edge (as shown in previous Section), position favored by the maxima in the magnetic field. As a consequence, all found vortex states for positive applied field are *multivortex states* (see left part of Fig. 5.4). As found earlier in this thesis, even $L = 1$ state shows unconventional asymmetry, in attempt to place the single vortex closer to the edge of the SC disk.

On the other hand, situation is quite different for negative applied magnetic field. As the stray field of the magnetic coating has opposite direction to the applied field in the SC disk, the compensation takes place. With increasing applied field, vortices (actually anti-vortices) start to nucleate in the sample only after maximal compensation is reached (in the present case, for $H = -0.66H_{c2}$). However, this maximal compensation *does not mean* that no magnetic field remains in the sample. Translated to the language of supercurrents, we could conclude the following: since the stray field induces supercurrents in the SC disk which have abrupt maximum at the disk edge (see Fig. 4.4), and homogeneous field induces opposite currents which are also maximal at the disk edge but broadly spread into the sample (see Sec. 1.2.2, the superposition of these currents results in a profile with maximum somewhat away from the edge of the SC disk. It is already well known that strong screening currents at the edges of small SC disks are responsible for the compression of existing vortices into the giant-vortex [1]. Since in our case strongest currents run even closer to the interior of the superconducting sample, we have found *only giant-vortex states* for all vorticities in applied negative field. Cooper-pair density and phase contourplots of some of this states are shown in Fig. 5.4 in the right panel.

To conclude, we observed here the field-polarity-dependent vortex structure in a SC disk with magnetic coating. Contrary to the case of uncoated SC disk where both multi- and giant- vortex states were found at unipolar field, we now find only multivortex (or giant-vortex) stable in applied positive (or negative) magnetic field.

5.3 VORTEX SHELLS AND CONTROL OF "MAGIC NUMBERS"

In the recent years, shell structure of vortex configurations in superconducting disks has drawn a lot of attention, particularly due to the analogy of this system to e.g. clusters of charged particles in parabolic confinement, electrons on liquid helium, dust in plasmas, and colloids. Vortices in small superconductors are a typical representative of interacting particles in finite systems (other examples are, e.g., electrons in artificial atoms [56] and vortices in

rotating superfluids [57]. Considering vortices as a pointlike object (i.e, the London approximation) it was predicted that they will obey specific rules for shell felling and exhibit magic number. But the situation is much complicated as they can overlap even can join together creating giant vortex state. The details of particle configurations in such systems, e.g., stability of different states or the rules of formation of consecutive shells of particles, are arising due to the competition between the effects of particle interactions and confinement [56, 57, 47]. Recent studies on vortex positions in mesoscopic disks established the prediction of vortex shell in some limiting case. Depending on disk radius the concept is like: (1) for small disk radii a single ring of vortices can be present [1, 14, 39], (2) for infinitely extended superconducting films where the triangular Abrikosov vortex lattice is energetically favorable [29, 30] and (3) in intermediate region rings (or shells) of vortices appeared with increasing radius [47, 58]. One may predict that for sufficiently large disk a triangular lattice is formed in the center.

Both experiment [58] and theory [47] have shown the formation of vortex shells in SC disks, where number of shells and number of vortices in each of them was dependent on the parameters of the system. Nevertheless, certain configurations appeared to be more stable than others, with particular numbers of vortices in neighboring shells, so-called "magic numbers". For example, it has been found that 19 vortices would form a (1,6,12) configuration in the ground-state, independently of other parameters. Also, more than 5 vortices in the very first shell were never found stable. In what follows, we will briefly address the issue of "magic numbers" in our system, i.e. SC disk with magnetic coating.

In the previous section, we discussed the effect of interplay between the stray field of the magnetic coating and the additional homogeneous magnetic field. In short, vortices favored positions closer to the edge of the SC disk in case when stray field and applied field were of same polarity, and vice versa. Fig. 5.5 shows the vortex configurations for different vorticities in a disk of radius $R = 14\xi$ and thickness $d = 0.5\xi$, with 1ξ thick magnetic coating with magnetization $M = -100H_{c2}$. While configurations in the left and right panel of Fig. 5.5 contain identical number of vor-

tices, they differ in the polarity of applied field with respect to the magnetization of the coating.

At zero applied field, no vortices were present in the sample, and superconductivity was somewhat suppressed at the disk edges, due to the stray field of the magnetic coating. For positive applied homogeneous field, the stray field at the edges is slowly being compensated. In any case, even small applied field creates several vortices in the superconductor (due to its large size), but is not able to fully overwhelm large amplitude of the stray field at the edges. For that reason, vortices avoid the periphery of the disk and are somewhat compressed towards the center of the SC disk. Nevertheless, their shell structure is not altered compared to the case of opposite magnetic field (or magnetization) since vortices have enough space to maintain their lowest-energy configuration [see Fig. 5.5(a,b)]. However, for large vorticities, i.e. $L > 35$, larger number of vortices falls under strong influence of the stray field of the magnetic coating. As a consequence, the shell structure changes. For example, one can see in Fig. 5.5(c) that for opposite polarity of the applied field, the structure of 53 vortices in our sample changes from (3,9,15,26) to (4,11,16,22). Therefore, the compression of vortices repelled by magnetic coating results in more vortices in the outmost shell and less vortices in the central region of the sample. As shown in Fig. 5.5(d), magnetic coating can even change the number of shells in the sample. For $L = 60$, we found configuration (4,10,16,30) at positive applied field, while ground-state at negative field for the same vorticity exhibits "magic numbers" configuration (1,6,12,18,23).

In conclusion, we have shown that magnetic coating can very effectively change the shell configuration of vortices in superconducting disks. We leave the very exhaustive analysis of all relevant parameters for some future work, as this topic is out of the scope of this thesis.
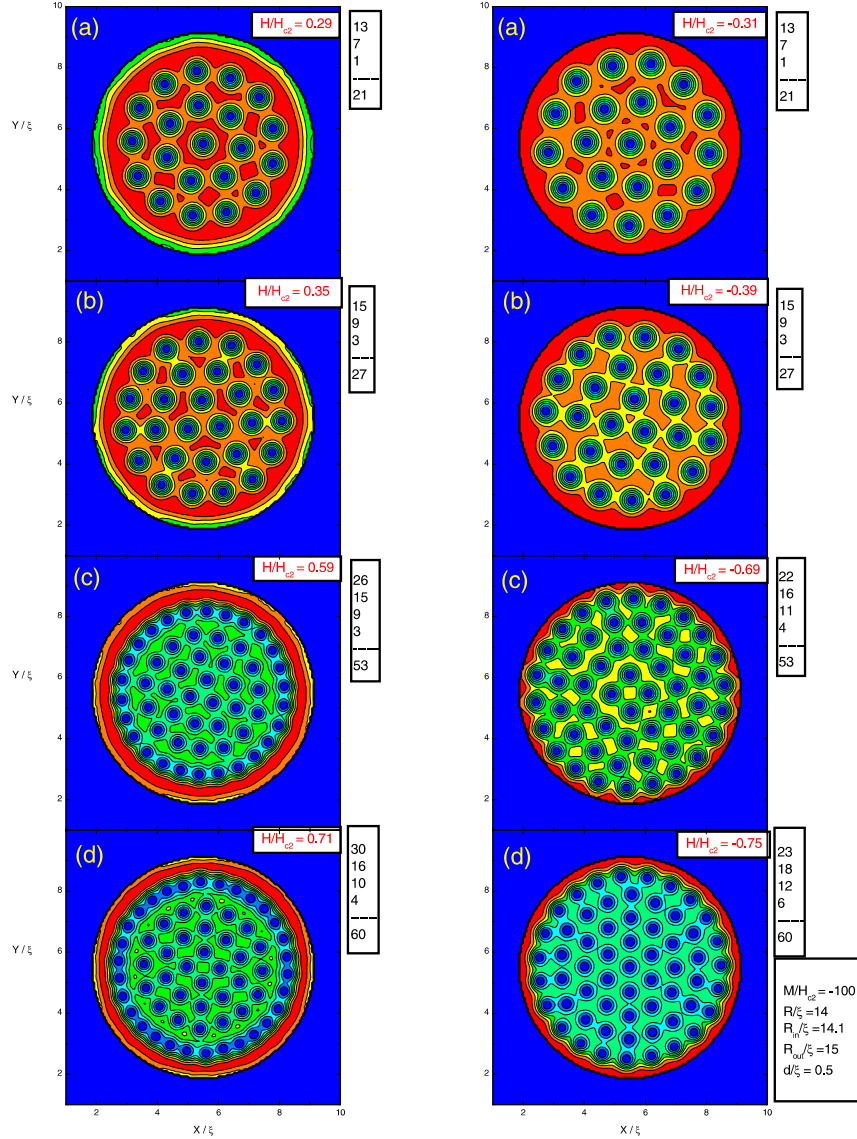
Fig. 5.5 Contourplots of the Cooper-pair density of the vortex configurations in the ground state, for vorticities 21(a), 27(b), 53(c), and 60(d), at positive (left panel) and negative (right panel) applied magnetic field.

6
Summary

In this thesis we investigated the hybrid superconductor(SC) /ferromagnet(FM) structure, where extreme type-II superconducting disk is surrounded by a thin ferromagnetic coating (i.e. a magnetic ring). Proximity effect between a superconductor and ferromagnetic element has been avoided, as they were separated by a thin oxide layer. The size of the whole sample is kept in a mesoscopic regime, i.e. comparable to the coherence length ξ and the magnetic penetration depth λ. The critical parameters and the vortex configurations of such samples are determined not only by the material and the quantum confinement imposed by small size of the structure, but also by the properties of the applied magnetic field (stray field of the magnet and/or homogeneous external field).

In what follows, our theoretical findings are summarized in order they are presented in the thesis.

In **Chapter 1**, a short introduction of superconductivity is provided. Important parameters and features of mesoscopic superconductors are discussed. An overview of the distribution of magnetic field, Cooper-pair density and supercurrent as well as the Gibbs free energy of a mesoscopic superconducting disk in homogeneous magnetic field is given as a reference point for the results in the following chapters.

We have focused in this thesis on the electromagnetic interaction between a superconductor (SC) and ferromagnet (FM), as a complex interplay between the energetics of a superconductor and the inhomogeneity of the stray field of the magnet [5, 32]. The basic magnetostatic calculations and stray field profile of a ferromagnetic ring with uniform magnetization along z direction is given in **Chapter 2**. Both the analytical and numerical approach have been presented. Our numerical approach is based on a superposition principle, where the field of a magnetic element of arbitrary shape has been expressed through the sum of fields emerging from a set of magnetic dipoles. The analytical approach [13] and numerical approach give results showing firm agreement. The main properties of the stray field of magnetic ring are discussed - having opposite polarity inside and under the ring, having extremes close to the inner edge of the ring, and a fast decay towards the center of the structure. Dependence of the field distribution on geometrical parameters of the ring was also analyzed.

In extreme type-II superconductors (with large Ginzburg-Landau parameter κ), the magnetic field generated by the circulating superconducting currents can be neglected, and the total magnetic field equals the applied one. Based on this condition, only first GL equation was solved in **Chapter 3**, with assumption of cylindrical symmetry of the superconducting state. In this one-dimensional approach, giant vortex state is an imposed solution for any vorticity. Our results show that for small SC disk radii only Meissner state is favorable in the ground state, even for large magnetization of the surrounding FM ring up to the critical one. In case of larger SC disk, the free energy shows a counterintuitive re-entrant behavior, where $L = 0 \rightarrow 1 \rightarrow 0$ transition occurs in the ground state with increasing magnetization of the FM coating. Sufficiently large magnetic field completely suppresses the Cooper-pair density at the edge exhibiting the ring-vortex-like distribution of the order-parameter. However, there are no vortices present in the sample, and this Cooper-pair distribution enables the Meissner state to become the ground state again, now at large magnetic field. This behavior was never found in the case of SC disks in applied homogeneous field [46, 1], and is therefore very counterintuitive and interesting.

However, it is well-known that large superconducting samples favor vortex configurations comprising individual vortices, i.e. the mesoscopic analogue of the Abrikosov lattice. Therefore, we employed the two-dimensional approach in **Chapter 4**, where the cylindrical symmetry of the vortex state is not taken a priori. The first results did not confirm reentrance of Meissner phase in the ground-state. Instead, the free-energy diagram showed successive entry of vortices in the sample with increase of the magnetization of the FM-coating. But, vortex configurations exhibited several novel features. For one, the $L = 1$ state showed unconventional behavior. Although single vortex was always found favorable to sit in the disk center for small disks (i.e. strong lateral confinement), for large disk radius due to the competition between the stray magnetic field and topological confinement, asymmetry in vortex position is realizable. To emphasize, this feature is very counterintuitive and not possible in the case of SC disk in a homogeneous magnetic field. Vortex configurations of higher angular momenta are multivortex states, with single vortices located close to the maximal stray field region. Thus accordingly to the spatial stray field profile of the FM ring, vortices are arranged in a shell close to the edge of the disk.

Interestingly enough, our calculation shows that after certain maximal number of vortex lines in the disk with given radius is reached, vortices start to gradually leave the sample in increasing magnetic field, and state with just suppressed order parameter at the disk edge becomes the ground state. This "Meissner" state (since it contains no vortices) corresponds to the one found in Chapter 3, and confirms found reentrance of $L = 0$ state in the ground state. Our results show that $L = 0$ state actually has two separate manifestations, the conventional Meissner phase at low applied field, and the phase showing novel ring-like suppression of superconductivity at disk edges at high magnetic field. However, one should note that this ring-like singularity of the order-parameter does not correspond to the ring-vortex predicted in Refs. [5, 61], as this excited state was not found stable in our case. Instead, the fact that the order parameter vanishes at the edge effectively modifies our boundary conditions from Neumann to Dirichlet case. Consequently, as shown in Ref. [48], additional

vortex entry is not possible, and superconductivity is completely destroyed with increasing magnetization of the coating further.

Chapter 5 deals with samples discussed in previous sections but additionally exposed to a homogeneous magnetic field. Response of different SC-FM structures to such external field has been studied earlier (Refs. [5, 2, 3, 9] etc.) in terms of vortex pinning, enhancement of critical parameters, and field-induced-superconductivity. We showed that the upper critical field of our sample can be engineered for given polarity of the applied magnetic field by proper choice of the parameters of magnetic coating. In addition, the polarity of applied field was also important for the resulting vortex structure. When magnetization of the FM coating and the applied field were taken parallel, due to low resulting total magnetic field at the disk edge (stray field of the coating compensates the applied one), vortices favor central position in the disk and merge into a giant vortex, whereas for opposite polarity of the applied field, multi-vortex state is the ground state. Contrary to Chapter 4, individual vortices can now enter the center of the disk in the latter case, since a non-zero total field exists in the interior. As a consequence, another ring of internal vortices can be formed, which can even become a giant-vortex depending on the parameters of the sample.

The formation of multiple vortex shells is not surprising and has been observed before in large SC disks in homogeneous field [47, 58]. However, our system offers potential control of so-called "magic numbers", i.e. the number of vortices in each shell. As we show in the last paragraphs of the thesis, FM coating around the SC disk forces present vortices either to avoid or sit closer to the edge, and strongly influences the exact arrangement of vortices in particular shells, even the number of shells at given vorticity. One should note that in disks in homogeneous magnetic field, number of shells and number of vortices in them are strictly defined in the ground-state by the radius of the disk [47, 58].

References

1. V. A. Schweigert and F. M. Peeters, Phys. Rev. B **57**, 13817 (1998).

2. I. F. Lyuksyutov and V. L. Pokrovsky, Adv. Phys. **54**, 67 (2005).

3. M. Lange, M. J. Van Bael, and V. V. Moshchalkov, J. Low Temp. Phys. **139**, 195 (2005) .

4. M. V. Milošević and F. M. Peeters, J. Low Temp. Phys., **139**, 257 (2005).

5. M. V. Milošević, *"Vortex Matter in Mesoscopic Supercon-ductor/Ferromagnet Heterosystems"* PhD thesis, University Antwerpen (2004).

6. I. K. Marmorkos, A. Matulis, and Peeters F. M., Phys. Rev. B **53**, 2677 (1996).

7. M. V. Milošević, S. V. Yampolskii, and F. M. Peeters, Phys. Rev. B **66**, 174519 (2002).

8. A. Hubert and R. Schäfer, *"Magnetic domains"* Springer, Berlin, (2000).

9. D. S. Golubović, M. V. Milošević, F. M. Peeters, and V. V. Moshchalkov, Phys. Rev. B **71**, 180502 (R) (2005).

10. M. Marchevsky, L. A. Gurevich, P. H. Kes, and J. Aarts, Phys. Rev. Lett. **75**, 24002403 (1995).

11. A. Kanda, B. J. Baelus, F. M. Peeters, K. Kadowaki, and Y. Ootuka, Phys. Rev. Lett. **93**, 257002 (2004).

12. J. D. Jackson: *"Classical Electrodynamics"* (John Wiley and Sons Inc. New York, (1975).

13. Y. L. Hao, *"Numerical Simulation of the Electrical response of a Ballistic Hall Bar in the presence of an Inhomogeneous Magnetic Field Profile"* Master thesis, Antwerpen University (2006).

14. V. A. Schweigert, F. M. Peeters, and P. Singha Deo, Phys. Rev. Lett B **81**, 2783 (1998).

15. Soltan Eid Abdel-Gawad Soltan, *"Interaction of Superconductivity and Ferromagnetism in YBCO/LCMO Heterostructures"* PhD thesis Max-Planck Institute, Stuttgart, (2005).

16. A. Schilling, M. Cantoni, J. D. Guo, and H. R. Ott, Nature **363**, 56 (1993).

17. S. N. Putilin, E. V. Antipov, A. M. Abakumov, M. G. Rozova, K. A. Lokshin, D. A. Pavlov, A. M. Balagurov, D. V. Sheptyakov, and M . Marezio, Physica C **383**, 52 (2000).

18. H. Kamerlingh Onnes, Commun. Phys. Lab. **12**, 120 (1911).

19. W. Meissner and R. Ochsenfeld, Naturwiss. **21**,787 (1933).

20. F. London and H. London, Proc. Roy. Soc. **A149**, 71 (1935).

21. V. L. Ginzburg and L. D. Landau, Zh. Eksperim.i. Theory. Fiz **20**, 1064 (1950).

22. A. A. Abrikosov, Sov. Phys. JETP **5**, 1174 (1957).

23. J. Bardeen, L. N. Cooper and J. R. Schrieffer, Phys. Rev. **108**, 1175 (1957).

24. L. P. Gor'kov, Sov. Phys. JETP **9**, 1364 (1959).

25. J. G. Bednorz and K. A. Müller, Z. Phys. B **64**, 189 (1986).

26. L. D. Landau and E. M. Lifshitz, *"Statistical Physics"* 3rd edn, part1 (Pergamon Press, Oxford, 1980).

27. E. Akkermans and K. Mallick, J. Phys. A **32**, 7133 (1999).

28. L. N. Cooper Phys. Rev. **104**, 1189 (1956).

29. P. G. de Gennes, *"Superconducting of Metals and Alloys"* (Benjamin, New York, 1966).

30. M. Tinkham, *"Introduction to Superconductivity"* (McGraw Hill, New York, 1975).

31. V. V. Schmidt, P. Müller, and A. V. Ustinov: *"The physics of Superconductors: Introduction to Fundamentals and Applications"* (Springer-Verlag, Berlin Heidelberg, 1997).

32. Dušan Golubović, *"Nucleation of superconductivity and vortex matter in superconductor / ferromagnet nanostructures"* PhD thesis, Katholic University Leuven, Belgium, (2005).

33. SØren P. Madsen, *"Flux Dynamics in High Tc Superconductors"* PhD thesis, Denmark Technical University (DTU) (2006).

34. L. Neumann and L. Tewordt, Z.Phys. **189**, 55 (1966).

35. B. J. Baelus, F. M. Peeters, and V. A. Schweigert, Phys. Rev. Lett B **61**, 9734 (2000).

36. A. C. Rose-innes and E. H. Rhoderick: *"Introduction to superconductivity"* (pergamon Press, Oxford, 1969).

37. Y. A.Genenko, H. Rauh, and S. V.Yampolskii, *"The Bean-Livingston barrier at a superconductor/magnet interface"* (pergamon Press, Oxford, 1969).

38. Bedanov and Peeters, Phys. Rev. B **49**, 2667 (1994).

39. P.S.Deo, V. A. Schweigert, F. M. Peeters, and A. K. Geim, Phys. Rev. Lett **79**, 4653 (1997).

40. L. F. Chibotaru et al, Nature **408**, 833 (2000).

41. A. I. Buzdin and J. P. Brison, Phys. Rev. Lett A **196**, 267(1994).

42. O. Fischer *"Magnetic Superconductors in Ferromagnetic Materials"* (North-Holland, Amsterdam, 1990) pp. 465-549.

43. S. V. Yampolskii and F. M. Peeters, Phys. Rev. Lett B **62**, 9663 (2000).

44. R. Kato,Y. Enomoto, and S. Maekawa, Phys. Rev. B **47**, 8016 (1993).

45. Yu. A. Genenko, A. Snezhko, and H. C. Freyhardt, Phys. Rev. B **62**, 3453 (2000).

46. Ben Baelus *"Vortex Matter in Mesoscopic Superconductors"* PhD thesis, University Antwerpen (2002).

47. B. J. Baelus, L. R. E. Cabral, and F. M. Peeters, Phys. Rev. B **69**, 064506 (2004).

48. Alexander D. Hern*ández* and Deniel Dominguez, Phys. Rev. B **65**, 144529 (2002).

49. L. R. E. Cabral, B. J. Baelus, and F. M. Peeters, *"From vortex molecules to the Abrikosov lattice in thin mesoscopic superconducting disks"* Phys. Rev. B **70**, 144523 (2004).

50. B. J. Baelus, A. Kanda, F. M. Peeters, Y. Ootuka, and K. Kadowaki, *"Giant and multivortex states in mesoscopic superconducting disks"* Physica C **426-431**, 132-135 (2005).

51. Martin Lange, Margriet J. Van Bael, Yvan Bruynseraede, and Victor V. Moshchalkov, *"Nanoengineered Magnetic-Field-Induced Superconductivity"* Phys. Rev. Lett. **90**, 197006 (2003).

52. A. K. Geim et al, Nature **396**, 144 (1998).

53. A. Kanda et al, Phys. Rev. Lett. **93**, 257002 (2004).

54. A. K. Geim et al, Phys. Rev. Lett. **85**, 1528 (2000).

55. A. K. Geim et al, Nature **407**, 55 (2000).

56. V. M. Bedanov and F. M. Peeters, Phys. Rev. B **49**, 2667 (1994).

57. L. J. Campbell and R. M. Ziff, Phys. Rev. B **20**, 1886 (1979).

58. I. V. Grigorieva, L. Y. Vinnikov1, W. Escoffier, J. Richardson, S. V. Dubonos, V. Oboznov , A. K. Geim. Phys. Rev. Lett. **96** 077005 (2006).

59. Jos I. Martn, M. Vlez, A. Hoffmann, Ivan K. Schuller, and J. L. Vicent, Phys. Rev. Lett. **83**, 1022 (1999).

60. G. R. Berdiyorov, M. V. Milosevic and F. M. Peeters, Europhys. Lett. 74 (3), pp. 493-499 (2006).

61. E. Akkermans and K. Mallick, J. Phys. A **32**, 7133 (1999).